

Catalytic routes to fuels from C₁ and oxygenate molecules

Shuai Wang, Iker Agirrezabal-Telleria, Aditya Bhan,[†] Dante Simonetti,[‡] Kazuhiro Takanabe[§] and Enrique Iglesia^{*}

Received 16th January 2017, Accepted 20th January 2017

DOI: 10.1039/c7fd00018a

This account illustrates concepts in chemical kinetics underpinned by the formalism of transition state theory using catalytic processes that enable the synthesis of molecules suitable as fuels from C₁ and oxygenate reactants. Such feedstocks provide an essential bridge towards a carbon-free energy future, but their volatility and low energy density require the formation of new C–C bonds and the removal of oxygen. These transformations are described here through recent advances in our understanding of the mechanisms and site requirements in catalysis by surfaces, with emphasis on enabling concepts that tackle ubiquitous reactivity and selectivity challenges. The hurdles in forming the first C–C bond from C₁ molecules are illustrated by the oxidative coupling of methane, in which surface O-atoms form OH radicals from O₂ and H₂O molecules. These gaseous OH species act as strong H-abstractors and activate C–H bonds with earlier transition states than oxide surfaces, thus rendering activation rates less sensitive to the weaker C–H bonds in larger alkane products than in CH₄ reactants. Anhydrous carbonylation of dimethyl ether forms a single C–C bond on protons residing within inorganic voids that preferentially stabilize the kinetically-relevant transition state through van der Waals interactions that compensate for the weak CO nucleophile. Similar solvation effects, but by intrapore liquids instead of inorganic hosts, also become evident as alkenes condense within MCM-41 channels containing isolated Ni²⁺ active sites during dimerization reactions. Intrapore liquids preferentially stabilize transition states for C–C bond formation and product desorption, leading to unprecedented reactivity and site stability at sub-ambient temperatures and to 1-alkene dimer selectivities previously achieved only on organometallic systems with co-catalysts or activators. C₁ homologation selectively forms C₄ and C₇ chains with a specific backbone (isobutane, triptane) on solid acids, because of methylative growth and

Department of Chemical Engineering, University of California at Berkeley, Chemical Sciences Division, E. O. Lawrence Berkeley National Laboratory, Berkeley, CA 94720, USA. E-mail: iglesias@berkeley.edu

[†] Current address: Department of Chemical Engineering and Materials Science, University of Minnesota, Minneapolis, MN 55455.

[‡] Current address: Department of Chemical and Biomolecular Engineering, University of California at Los Angeles, Los Angeles, CA, 90095.

[§] Current address: King Abdullah University of Science and Technology, KAUST Catalysis Center, Physical Science and Engineering Division, Thuwal, 23955, Saudi Arabia.

hydride transfer rates that reflect the stability of their carbenium ion transition states and are unperturbed by side reactions at low temperatures. Aldol condensation of carbonyl compounds and ketonization of carboxylic acids form new C–C bonds concurrently with O-removal. These reactions involve analogous elementary steps and occur on acid–base site pairs on TiO₂ and ZrO₂ catalysts. Condensations are limited by α -H abstraction to form enolates *via* concerted interactions with predominantly unoccupied acid–base pairs. Ketonization is mediated instead by C–C bond formation between hydroxy-enolates and monodentate carboxylates on site pairs nearly saturated by carboxylates. Both reactions are rendered practical through bifunctional strategies, in which H₂ and a Cu catalyst function scavenge unreactive intermediates, prevent sequential reactions and concomitant deactivation, and remove thermodynamic bottlenecks. Alkanal–alkene Prins condensations on solid acids occur concurrently with alkene dimerization and form molecules with new C–C bonds as skeletal isomers unattainable by other routes. Their respective transition states are of similar size, leading to selectivities that cannot sense the presence of a confining host. Prins condensation reactions benefit from weaker acid sites because their transition states are less charged than those for oligomerization and consequently less sensitive to conjugate anions that become less stable as acids weaken.

1. Background and context

The role of catalysis, and specifically of processes enabled by heterogeneous catalysts, in the conversion and upgrading of molecules intended for use as fuels and energy carriers has been remarkable in breadth and impact¹ throughout nearly a century of symbiotic relationships between concepts and technologies that have evolved side-by-side. In fact, together with the engineering and design of chemical processes, the science and practice of heterogeneous catalysis have been critical in the evolution of modern-day fuels by enabling their improved performance and environmental compatibility; catalysis and its fundamental concepts and tools will remain so as we evolve from crude oils to transitional sources of fuels and feedstocks, such as natural gas² and biomass,³ and ultimately to carbon-free energy carriers derived from geothermal, wind, and solar resources.

Even a cursory review of such a storied history would be impossible; it is not the intent of this brief and modest account. Instead, the discourse focuses on conceptual advances in upgrading streams derived from natural gas – C₁ molecules that lack C–C bonds – or from oxygenates of plausible biogenic origins. We have chosen, as a matter of comfort and uniformity, illustrative case studies from our research group. The emphasis on concepts in each section is intentional, without any intent to distract the reader from the realities of heterogeneous catalysis as a discipline with a historical record of formidable practical impact.

Low volatility and high energy density are primary characteristics of transportation fuels, imparted in current refining strategies by conversion and upgrading units. C₁ molecules, typified by CH₄, the molecule with the highest energy density per C-atom, lack C–C bonds. Oxygenates, in turn, lack the required energy density, and O-removal forms carbon chains that are too short to meet volatility requirements, thus requiring the concurrent formation of new C–C bonds during O-removal. Appropriately, therefore, what follows focuses on the formation of new C–C bonds (homologation, carbonylation, oligomerization) and

deoxygenation steps that concurrently form C–C bonds (aldol and Prins condensations, ketonization) as the enabling catalytic routes.

2. Catalysis for the conversion and upgrading of diverse feedstocks without C–C bonds and the challenges inherent in activation of C₁ molecules

The recurring interest in unconventional carbon sources as precursors to chemicals and transportation fuels periodically returns the catalysis field to the challenges of converting molecules, such as methane, methanol, and dimethyl ether, which lack C–C bonds. Such C₁ species, and methane specifically, bring forth formidable thermodynamic and kinetic challenges in directing the catalytic route towards products of higher value and practical use as fuels or chemicals. Such inherent hurdles and bottlenecks, with roots in thermodynamics but transferred into the realm of dynamics through linear free energy relations, lead to the significant complexity and cost that characterize the commercial deployment of C₁ conversion to more valuable molecules. Here, we discuss a conceptual framework to provide guidance for addressing these challenges in the form of some examples. In doing so, the reader will notice that we evolve the products of C₁ conversion from C₂ (oxidative coupling, carbonylation) to C₄ (dimerization) and ultimately C₄–C₇ (homologation) chains. The manuscript excludes, as a result of space constraints, any discussion of C₁ polymerization processes known as the Fischer–Tropsch synthesis and specifically of our recent studies of the unique reactivity and selectivity conferred upon catalytic surfaces by the presence of dense adlayers of chemisorbed CO.

2.1. Oxidative coupling of methane: selectivity conferred by strong H-abstractors formed *in situ* from O₂–H₂O mixtures

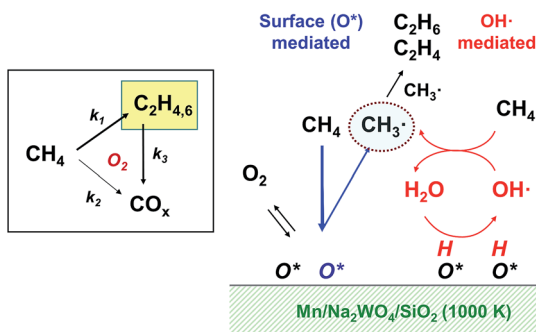
The kinetic consequences of ubiquitous thermodynamic hurdles in activating strong bonds preferentially over weaker ones, the inherent limitations of catalysis in circumventing them, and the pre-eminent requirement for processes that stress simplicity and inexpensive oxidants, such as O₂, are illustrated by the extensive studies of the process known as the oxidative coupling of methane (OCM). Here, we discuss how H-abstractors stronger than O₂, but formed *in situ* in the form of OH radicals from H₂O–O₂ mixtures, are used to moderate the kinetic preference for abstracting H-atoms from C–H bonds in C₂H₆ products instead of CH₄ reactants; these homogeneous activation routes also circumvent surface routes that favor unselective oxidation of even the stronger bonds in C₂H₄ because of their strong π -interactions with oxide surfaces.

OCM leads to the direct formation of a C–C bond from C₁ molecules *via* the coupling of two hydrocarbon radicals; it is favored under CH₄-rich conditions that tend to minimize the CO_x formation that prevails at combustion-type conditions. OCM involves coupled heterogeneous–homogeneous reactions, in which a C–H bond in CH₄ is activated *via* H-abstraction with O₂-derived surface species to form H₂O and gaseous CH₃ radicals that undergo subsequent homogeneous coupling reactions to form C₂H₆.⁴ The subsequent transformation of C₂H₆, which contains weaker C–H bonds than those in CH₄, proceeds *via* H-abstraction steps similar to those for CH₄ to form reactive species that ultimately form CO_x and C₂H₄. Such

pathways, described schematically in Scheme 1, limit attainable C_2 yields,^{5,6} because the conversion of C_2 products is more facile than that of CH_4 on oxide surfaces at the temperatures required to form the required CH_3 radical intermediates.

A detailed kinetic and isotopic study of OCM primary and secondary reactions on $Mn/Na_2WO_4/SiO_2$ ⁷ provided a rigorous mechanistic interpretation of the effects of H_2O in enhancing rates through parallel homogeneous activation routes involving OH radicals; such radicals were formed at oxide surfaces *via* reactions of H_2O (added or formed during OCM as CH_4 conversion increased) with O_2 -derived surface O^* species, as depicted schematically in Scheme 1^{8,9} and demonstrated experimentally from the higher C_2 yields attainable in the presence of the H_2O formed as the reaction proceeds (Fig. 1). Such parallel OH-mediated routes contribute significantly to C_2 formation rates and selectivities on such alkali-promoted catalyst compositions, which tend to show lower reactivity for C–H bond activation than Li–MgO and Sr–La₂O₃ compositions, on which surface-mediated routes prevail at their lower operating temperatures.

Isotopic tracer studies using mixtures of $^{13}CH_4/O_2$ with $^{12}C_2H_6$ or $^{12}C_2H_4$ in the presence or absence of added H_2O showed that H_2O increases the activation rates for all C–H bonds (k_1 , k_2 , and k_3), but to a different extent, thus leading to lower k_3/k_1 ratios (Fig. 2), consistent with the higher attainable C_2 product yields with added H_2O (Fig. 1).^{8,9} H-abstraction by OH radicals occurs less selectively for the weaker C–H bonds in C_2H_6 than for the stronger CH_4 bonds than in drier environments, in which surface O^* species carry out the required H-abstractions. In the absence of added H_2O , C–H bonds in C_2H_4 were more reactive than in CH_4 in spite of their greater strength (Fig. 2), but gave rate constant ratios slightly below unity when H_2O was added, as expected from stronger C–H bonds in C_2H_4 than CH_4 . Such kinetic models illustrate the essential effects of H_2O in enabling higher C_{2+} yields, as shown in Fig. 1. The blue data points in Fig. 1 correspond to these ratios of rate constants for C–H activation by surface O^* species (dry), while the red data points consider the additional contributions to such ratios by C–H activation mediated by OH radicals in the gas phase (wet).



Scheme 1 Simplified scheme for the OCM reaction network and pseudo-first-order rate constants for each step (left); representative scheme for OCM reaction steps involving CH_3 radical generation *via* surface O^* mediated (dry) and OH radical gas-phase mediated (wet) pathways on $Mn/Na_2WO_4/SiO_2$ (right).

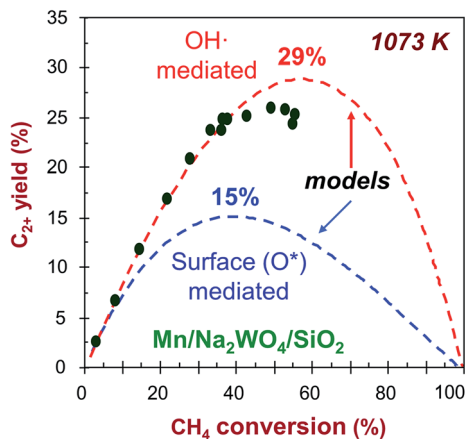


Fig. 1 Measured C_{2+} yields as a function of CH_4 conversion (data points) and model predictions from measured rate constants in this figure and the reaction steps in Scheme 1. Blue curve for surface O^* -mediated (dry) route and red curve for combined paths mediated by surface O^* (dry) and OH radicals (wet) routes (0.02 g, 1073 K, 4.0 kPa CH_4 , 1.3 kPa O_2 (initial), 1.5 kPa O_2 (added)). Adapted with permission from ref. 8 (Copyright 2008 Wiley-VCH).

These data suggest the involvement of parallel C–H activation routes (Scheme 1) involving pathways in which H-abstraction is mediated by either oxygen species on surfaces or by OH radicals, formed *via* H_2O/O_2 equilibration on catalyst surfaces, with specific involvement of Na or K cations.¹⁰ These coupled homogeneous-catalytic sequences are consistent with the kinetic effects of O_2 , CH_4 , and H_2O on the rates of primary and secondary reactions and with the observed H/D isotope effects. These isotopic data also show that C–H activation is irreversible and kinetically-relevant and that O_2 dissociation is quasi-equilibrated for surface routes, but becomes irreversible as O_2/H_2O ratios increase.

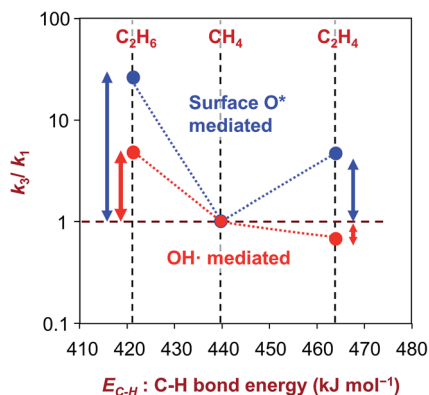


Fig. 2 The abscissa shows the C–H bond energies for CH_4 , C_2H_6 , and C_2H_4 . The lower measured k_3/k_1 rate constants for C–H bond activation in ethene or ethane (k_3) and methane (k_1) (as defined in Scheme 1) *via* surface O^* (dry) and gas-phase OH radical gas-phase (wet) pathways lead to the higher C_{2+} yields achieved with added H_2O (Fig. 1).

OCM rates and C_{2+} yields are higher when H_2O is present because these homogeneous OH-mediated pathways involve a much stronger H-abstractor than $O_2(g)$ or surface O^* species. Indeed, the ratio of pseudo-first-order rate constants for the activation of CH_4 to that for C_2H_6 increased monotonically and roughly exponentially as the enthalpy of the H-abstraction step increases for homogeneous H-abstraction reactions (Fig. 3),⁸ thus rendering OH radicals less selective for weaker C–H bonds than lattice O-atoms. Such trends reflect C–H activation transition states that occur earlier along the reaction coordinate as steps become more exothermic, leading to reactant-like structures in which C–H bonds are less fully cleaved and to activation barriers that are therefore less sensitive to the strength of the C–H bonds. Soft abstractors and low temperatures are often invoked as promising strategies to improve attainable C_2 yields in OCM; such strategies are not only incompatible with each other, but in fact counterproductive, because they strengthen the sensitivity of activation barriers to C–H bond strength. These concepts have been recently confirmed for the selective dehydrogenation of C_2H_6 with O_2/H_2O co-reactants.¹¹

2.2. Anhydrous carbonylation of dimethyl ether: confinement of transition states within inorganic pockets of molecular dimensions and the selective formation of a single C–C bond

The intended formation of C–C bonds from stable CH_4 molecules *via* the OCM routes in Section 2.1 illustrates the inherent challenges in the selective formation of the first C–C bond from C_1 molecules. The carbonylation of C_1 species forms such C–C bonds, but becomes thermodynamically possible only for oxygen-containing C_1 molecules, such as CH_3OH or CH_3OCH_3 (dimethyl ether, DME).

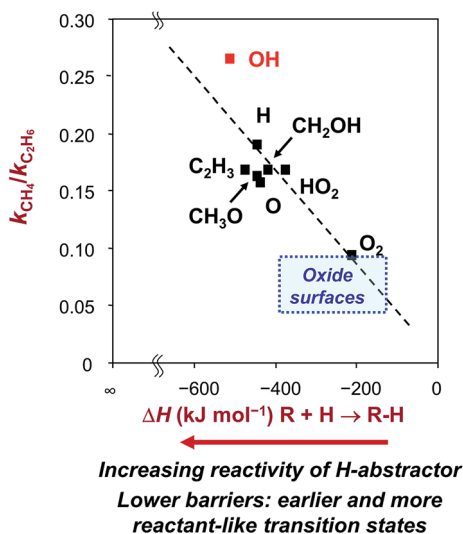


Fig. 3 Rate constant ratios for H-abstraction from CH_4 and C_2H_6 (1073 K, $k_{CH_4}/k_{C_2H_6}$) for different abstractors (R) as a function of the reaction enthalpy (ΔH for $R + H = R-H$). Data points are for homogeneous reactions of each R radical; the rectangle indicates range of H-abstraction properties of O^* . Adapted with permission from ref. 8 (Copyright 2008 Wiley-VCH).

In fact, such carbonylation reactions provide the only known route to form one single C–C bond with nearly perfect selectivity from two C₁ species. Current processes require the use of halides to form methylating species capable of reacting with a very weak nucleophile such as CO and organometallic complexes of Rh or Ir as catalysts, as implemented in the large-scale synthesis of acetic acid from CH₃OH–CO reactants.¹² These processes also require the exhaustive removal of H₂ from CO-containing streams to prevent deleterious side reactions that detract from selectivity and catalyst stability and lead to costly purification of product streams.

Efforts to catalyze CO reactions with CH₃OH on acid-forms of zeotypes led to very low rates and fast deactivation, symptomatic of competing hydrolysis reactions of bound methyls with H₂O molecules formed *via* fast CH₃OH homologation and dehydration reactions and of the need, unrecognized at the time, for voids of specific size in order to compensate for the weak nucleophilic character of CO. These hurdles were surmounted by the use of DME as the substrate, which allows carbonylation to occur under essentially anhydrous conditions with the consequent formation of methyl acetate (MeOAc), and by the discovery that side pockets in MOR structures and the smaller channels in two-dimensional networks in FER zeolites, both consisting of structures formed by inorganic rings containing eight O-atoms (eight-membered ring, 8-MR), provide effective van der Waals contacts with the transition state that mediates the formation of the C–C bond in the kinetically-relevant step.^{13–15} Such catalytic routes allow the direct use of synthesis gas to form a product (methyl acetate) that can be converted, if so warranted by markets, to acetic acid *via* reactions with H₂O or by coupling of CH₃OH dehydration (to DME) with MeOAc hydrolysis. MeOAc forms with >99% selectivity on these catalysts at moderate temperatures (<550 K); it can be used to form ethanol *via* hydrogenolysis and ethene *via* ethanol dehydration, thus providing the only known routes for the formation of molecules containing a single C–C bond from C₁ feedstocks.

DME carbonylation involves a kinetically-relevant step consisting of backside attack by CO on DME-derived methyls bound at Al sites on the acid-forms of zeotypes (Fig. 4). This mechanism is consistent with kinetic and isotopic data and with infrared spectra, as well as with the stoichiometric formation of CH₃ groups from DME and their subsequent reaction with CO and scavenging of acyls formed by another DME molecule;^{13–15} it is also in agreement with theoretical treatments that followed these experimental demonstrations and mechanistic interpretations.^{16,17} This catalytic cycle (Fig. 4A) forms an acyl intermediate that cannot desorb without an intervening methoxylation event, in which acyls react with DME to desorb MeOAc and to re-form a bound CH₃. This step avoids the recurrence of the slow formation of such CH₃ species from DME, which, under anhydrous conditions, needs to occur only once as an initiation step in a long propagation cycle, in which CO backside attack (Fig. 4B) and methoxylation provide the propagation elementary steps. Turnover rates (per H⁺) were highest on MOR structures (Fig. 4C), but varied significantly among MOR samples prepared or treated using different protocols. Rates were lower on FER samples and essentially undetectable on aluminosilicates lacking 8-MR structures (BEA, MFI, FAU, SiO₂–Al₂O₃) (Fig. 4C).

Such inferences about the required structural motifs led to the use of spectroscopic and titration methods to determine the location of protons within

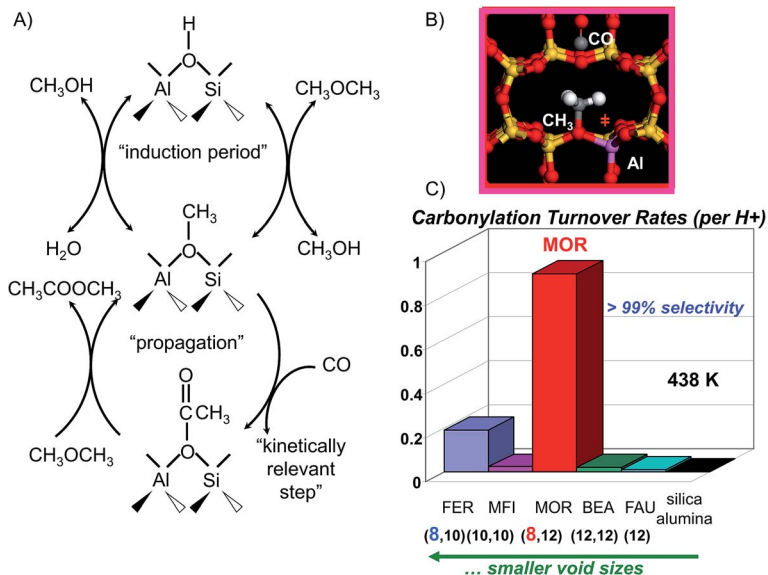


Fig. 4 (A) A proposed set of elementary steps describing the induction period and propagation reaction sequences in the carbonylation of dimethyl ether on proton form zeolites [adapted from Cheung *et al.*¹⁴]; (B) the transition state resembles a methyl carbenium ion stabilized via van der Waals interactions with the anionic zeolite framework and the carbon monoxide nucleophile [adapted from Neurock¹⁵]; (C) turnover rates (per proton) for dimethyl ether carbonylation (438 K, 0.93 MPa CO, 20 kPa DME, 50 kPa Ar) for H-form zeolites and amorphous silica alumina.

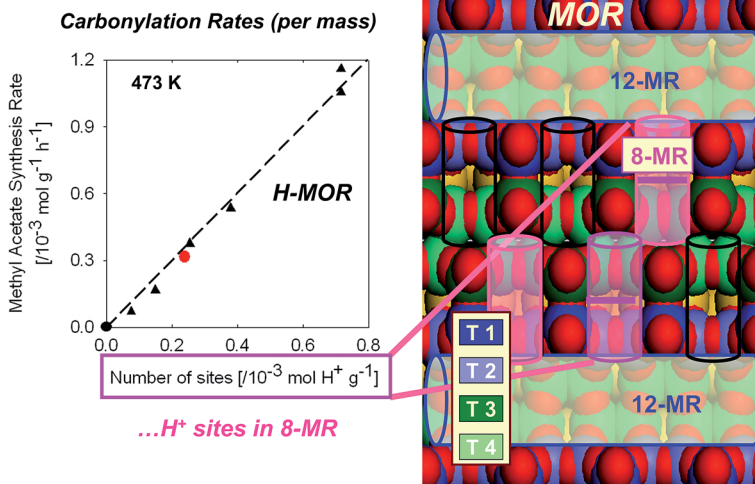


Fig. 5 DME carbonylation rates per unit mass (438 K, $3.34 \text{ cm}^3 \text{ s}^{-1} \text{ g}^{-1}$, 0.93 MPa CO, 20 kPa DME, 50 kPa Ar) plotted against the number of H⁺ sites per unit mass in 8-MR channels of Na-exchanged H-MOR (\blacktriangle ; Si/Al = 10, Zeolyst; Na/Al = 0.0–0.55) and Co-exchanged MOR (\bullet ; Co/Al = 0.65). Adapted from ref. 13.

different local environments in each given framework, as specifically in MOR, which exhibits the highest reactivity and in which protons reside at four crystallographically distinct locations that are located within two (8-MR and 12-MR) very different types of environments (Fig. 5). The use of pyridine as an organic titrant that can access only the 12-MR protons led to undetectable changes in rates, consistent with the kinetic irrelevance of H^+ species at 12-MR locations. The deconvolution of location-specific O–H infrared bands led to an accurate assessment of the fraction of protons at 8-MR and 12-MR locations. The rate data in Fig. 5 are plotted against the number of H^+ within 8-MR MOR structures for samples prepared or treated using different protocols or in which H^+ was exchanged for Na^+ to different extents. The excellent correlation between carbonylation rates and protons at 8-MR Al sites indicates that the relevant transition state structures are preferentially stabilized (relative to their bound CH_3 precursors) at 8-MR motifs that prevail in MOR and FER frameworks, while protons at Al sites within larger voids (10-MR, 12-MR motifs) exhibit much lower reactivity and lead to unselective homologation reactions. The specificity of such confinement effects for CH_3 reactions with CO was unprecedented at the time for inorganic solids, which predominantly influence reactivity by size exclusion of bulkier transition states or by restricting access and egress of certain molecules to the confining structures containing the active sites.

These stabilization effects depend on effective van der Waals contacts between the transition state and the confining voids and on such contacts being more effective for the backside CO-attack transition state than for its bound methyl precursors. Such enthalpic benefits of confinement prevail over the consequent entropic penalties because of the pre-eminent role of enthalpy in determining Gibbs free energies of activation at the moderate temperatures of DME carbonylation. As a result the best fit becomes a tight fit and the resulting solvation by the inorganic host preferentially stabilizes specific guests *via* dispersive forces. This preeminent role of dispersion becomes evident from carbonylation transition state enthalpies derived from density functional theory (DFT), which are not influenced by location when functionals that neglect such forces are used, but become favored at 8-MR locations when using either higher levels of theory or functionals that can account for non-specific induced dipole interactions.¹⁶

2.3. Dimerization and solvation by a liquid phase: selectivity for the formation of one C–C bond between ethene molecules and site stability conferred by intrapore liquids

The catalytic routes in the previous two sections have formed a single C–C bond from C_1 molecules, with different selectivities, at very different temperatures, and exploiting unrelated concepts and chemistries. This section shows that the chemistry required to form a single C–C bond between two ethene molecules (to form 1-butene) benefits from the preferential solvation of the C–C bond formation and product desorption transition states by an extended intrapore ethene liquid phase within MCM-41 channels that contain active Ni sites;¹⁸ such a liquid phase forms *via* capillary condensation at high pressures and sub-ambient temperatures (240–260 K).¹⁸ In this example, the host structure for the transition state guest is the mobile liquid solvent, in contrast with the quasi-rigid walls of microporous aluminosilicates in the DME carbonylation example of Section 2.2.

Heterogeneous ethene dimerization catalysts based on active Ni structures dispersed on mesoporous or microporous oxides typically require higher temperatures (380–500 K) to achieve rates similar to those observed at lower temperatures on homogeneous catalysts, but benefit from much less costly product-catalyst separation and from their ability to operate without activators or co-catalysts and to be regenerated without degradation, in contrast with homogeneous and MOF-based catalysts (Table 1). The higher temperatures required for oxide-based catalysts lead, however, to low 1-butene selectivities and to C₄ yield losses resulting from sequential oligomerization reactions; the latter reactions form larger chains that bind strongly to Ni active sites, thus requiring frequent thermal treatments for their removal *via* oxidation reactions or *via* the desorption of strongly-bound oligomers.

The operation of Ni-MCM-41 catalysts at pressures and temperatures that lead to the filling of MCM-41 mesopores with liquid ethene leads to a sharp decrease in their first-order deactivation rate constants (k_d , Fig. 6) and to a concomitant significant increase in catalyst life over those observed at higher temperatures in gas-filled mesopores (half-life reported as $1/k_d$; Table 1). Such stabilization becomes evident at relative ethene pressures of about 0.6 (defined as the ratio of ethene pressure to its saturation pressure at each temperature) (Fig. 6), which corresponds to that required for condensation within the 1.0–2.2 nm channels in MCM-41 (as determined from their pore-filling isotherms) where the active Ni sites are likely to reside. These liquid-filled channels lead to the conversion of ethene to 1-butene (1-C₄) with very high selectivity (98% butenes in products; 93% 1-butene in butenes) and with unprecedented turnover rates ($>10\text{ s}^{-1}$; per Ni atom), even at sub-ambient temperatures (243–258 K), without exhibiting detectable deactivation or requiring the aluminoxane activators essential for turnovers in homogeneous and Ni-MOF catalysts (Table 1).

Such unique reactivity, selectivity, and stability are imparted by the intrapore liquid phase, containing ethene and butene products, which preferentially

Table 1 Ethene dimerization rates, and C₄ and 1-butene selectivities for Ni-based catalysts

Catalyst	Ethene dimerization							
	Ni (% wt)	Pressure (MPa)	Temp. (K)	Rate ($\text{g}_{\text{butene}}/\text{g}_{\text{cat}}^{-1}\text{ h}^{-1}$)	Rate (per Ni atom) ($\text{g}_{\text{butene}}/\text{mol}_{\text{Ni}}^{-1}\text{ h}^{-1}$)	C ₄ in products (%)	1-Butene in C ₄ (%)	1/ k_d (h)
MOF ^{20a}	10.0	1.5	283	205	10 400	94 (95)	95	12
Ni-phosphine ^{19b}	—	6.0	298	—	26 600	9	50	—
FAU ^{22c}	3.7	1.5	388	10	530	53	—	65
MCM-41 ^{21,23d}	2.0	3.5	423	67	15 700	58	20	91
MCM-41 ^{18e}	0.2	3.0	258	43	38 900	98 (97)	92 (91)	630
	5.0	3.0	258	135	8700	98 (96)	93 (92)	612

^a *n*-Heptane solvent; Et₂AlCl activator (Al/Ni = 70). ^b Homogeneous α -nitroketonate Ni(II) complex; toluene solvent; MAO activator (Al/Ni = 100). ^c Ni-exchanged Na-FAU zeolite (Si/Al = 3); no solvent, full conversion. ^d Ni-exchanged Al/MCM-41 (Si/Al = 9); *n*-heptane solvent. ^e Ni-exchanged Al/MCM-41 (Si/Al = 40); no solvent at 5% (or 40%) conversion.

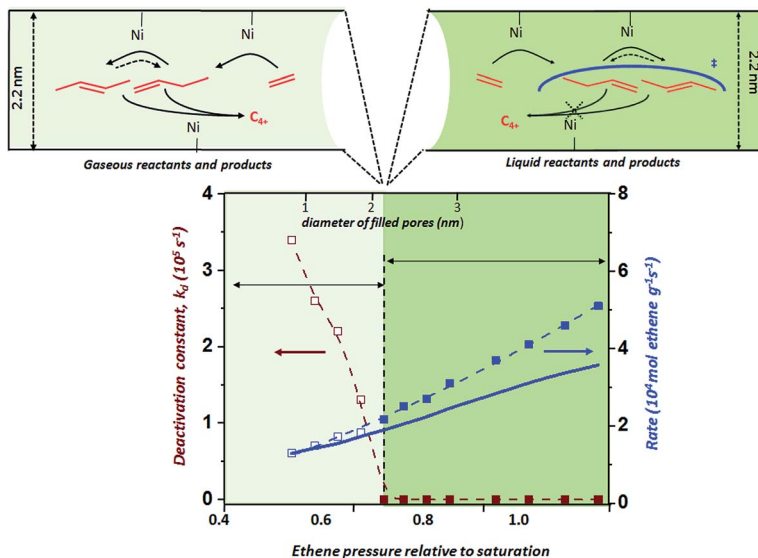


Fig. 6 Ethene dimerization first-order deactivation constant (k_d , data symbols, left), trend for deactivation constant (dashed, left), rates per catalyst mass (data symbols, right), trend for rates (dashed, right) and rates corrected by ethene fugacity (solid line, right) as a function of ethene pressure relative to saturation on 5.0% wt Ni-MCM-41 at 243 K. Symbols (\square) and (\blacksquare) denote conditions leading to intrapore gas and liquid, respectively. The top x-axis denotes the required MCM-41 pore diameter (2.2 nm) that leads to liquid reactants and products in pores containing exchanged Ni sites. The presence of intrapore liquids solvates the transition state that mediates the desorption of 1-butene and enables the transition from unstable to stable rates.

solvates the transition states that mediate the desorption of the primary 1-butene dimers before their isomerization or subsequent growth. Similarly, intrapore liquids derived from intrapore condensation of propene during its dimerization also lead to high rates and selectivities to hexenes and to stable operation conditions leading to capillary condensation (0.3 MPa, 260 K). These transition states occur late along the reaction coordinate, because of the endothermic nature of desorption processes; their product-like nature, resembling a desorbing alkene significantly interacting with the surrounding liquid phase, allows their preferential stabilization over strongly-bound transition states, which occur later along the reaction coordinate and mediate subsequent isomerization and oligomerization reactions of bound 1-alkenes formed as primary products in alkene dimerization elementary steps.

The remarkable stability of these materials in the presence of intrapore liquids allows the unequivocal attribution of reactivity to isolated Ni cations based on rates (per mass) that reach a constant value at a $\text{Ni}^{2+}/\text{H}^+$ exchange stoichiometry of unity, consistent with the plausible involvement of $\{\text{Ni}^{2+}-(\text{OH})^-\}^+$ species as active sites. Such stability also allows the mechanistic interpretation of dimerization rates in terms of elementary steps and of selectivity in terms of subsequent reactions that can occur during one surface sojourn at Ni sites or after 1-butene or its isomers readsorb along the catalyst bed with increasing residence time. Dimerization turnovers are limited by the reaction of a bound ethene, present at

low coverages at Ni sites, with an unbound ethene molecule, leading to rates that are approximately second order in ethene pressure. Transition state formalisms required to accurately treat chemical dynamics in thermodynamically non-ideal media show that the observed rate dependence on ethene fugacity, which is stronger than expected from bimolecular transition states, reflects the solvation effects by intrapore liquids, which lead to the kinetically-detectable stabilization of the C–C bond formation transition state. These intrapore hydrocarbon liquids, which are present without an extrapore continuous liquid flow in the catalyst bed, avoid potential leaching of Ni sites while leading to dimerization rates that are, in fact, significantly higher at sub-ambient temperatures than at the higher temperatures typically required for oxide-based Ni catalysts (Table 1). Solvation by liquids also increases the desorption of surface 1-butene, as a primary dimerization product, thus minimizing its conversion to regioisomers or to larger oligomers, and consequently increasing the selectivity to 1-butene regioisomers within butenes and to C₄ chains within products. These phenomena highlight, as in carbonylation catalysis, the enabling role of solvents, whether as inorganic hosts or extended liquids, in modifying reactivity and selectivity by stabilizing specific transition states, a subject examined again in Section 3.3 in the context of alkene–alkanal Prins condensations on acid-forms of zeotypes.

2.4. Methylative homologation of alkenes and alkanes using C₁ oxygenates: formation of highly branched alkanes *via* the orderly methylation and timely hydride transfer inherent in “undisturbed” carbenium ion reactions

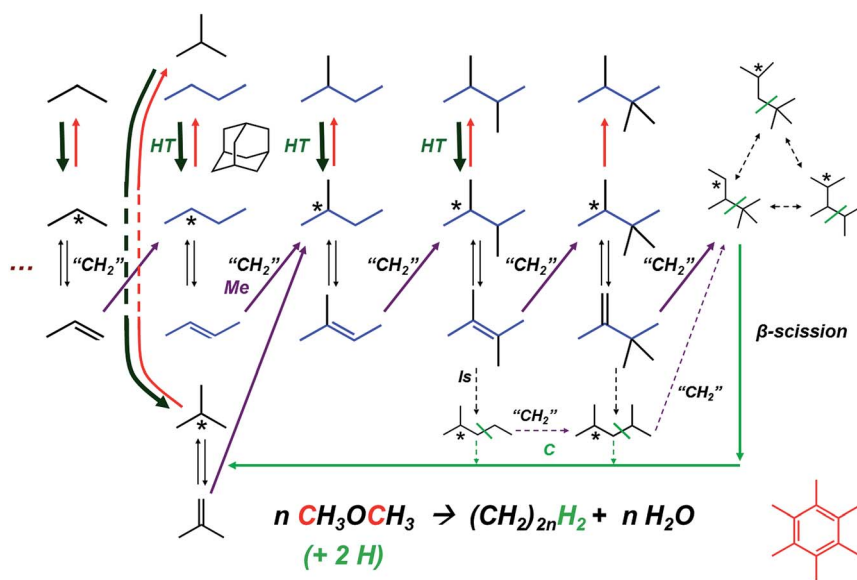
The catalytic strategies described in the previous three sections, as well as CH₃OH/DME homologation routes at high temperatures (>600 K),²⁴ lead to C₁-derived aliphatic and aromatic molecules with additional C–C bonds. Metathesis can then shuffle C–C bonds among alkenes to form chains of intermediate length,²⁵ including *via* tandem dimerization-metathesis strategies that can form alkenes with odd carbon numbers (*e.g.* propene from ethene).²⁶ Alkenes and alkanes can also grow into larger chains *via* oligomerization and alkylation processes on solid acids.²⁷ These strategies allow some modest control over the chain length and backbone structure in products, but the required temperatures typically lead to secondary skeletal isomerization and β-scission reactions; these secondary reactions lead to product slates diverse in chain length and backbone structure.

The remarkable ability of some metal halides in liquid methanol (*e.g.* Zn and In iodides) to form supra-equilibrium concentrations of triptane (2,2,3-trimethylbutane) and isobutane at low temperatures (400–500 K)^{28,29} led us to consider the use of solid acids at these lower temperatures but at higher DME pressures (60–250 kPa) than typically used in homologation of C₁ oxygenates *via* processes known as methanol-to-hydrocarbon chemistries.²⁴ In doing so, we uncovered the previously unrecognized ability of solid acids at these temperatures to also form triptane and isobutane with unprecedented selectivity,^{30–33} while also demonstrating the likely involvement of protons in the metal halide systems, where protons can form *via in situ* hydrolysis of halides by the H₂O formed in C₁ homologation steps. The resulting mechanistic insights, gained through extensive kinetic and isotopic tracer studies, provided a unique vantage point into the “rules” for methylation and hydride transfer reactions of bound alkoxide

intermediates.³¹ It also opened an unexpected opportunity to introduce unreactive light alkanes into homologation cycles, *via* chemistry that became known as methylative homologation of alkanes,³² thus fulfilling the hydrogen requirements for alkane formation from CH₃OH and DME and allowing the recycle of the isobutane products into the methylation–hydrogen transfer catalytic cycle.

In fact, the unique selectivities to isobutane and triptane reflect the preference of alkoxides to methylate at specific locations and to desorb *via* H-transfer when they reach a specific length and skeletal backbone structure along the methylation path. Preferential methylation occurs at positions that preserve a four-carbon backbone along the chain growth path merely because of the stability of the carbenium ion transition states that mediate methylation events (Scheme 2). Slow skeletal isomerization and β -scission reactions of these four-carbon backbone species prevent their deviation from the path to triptane, while fast isomerization and β -scission occur for any chains that grow beyond triptane with the consequent formation of isobutyl chains that desorb as isobutane. Facile hydrogen transfer to *tert*-butoxides and 2,3,3-trimethyl *sec*-butoxides relative to the methylation of isobutene and triptene causes these species to preferentially exit the chain growth sequence as isobutane and triptane.

These reactions are shown to occur on all solids containing Brønsted acid sites (Fig. 7)³³ and are mediated by carbenium ion transition states that favor methylation (instead of hydrogen transfer, isomerization, or cracking) when alkoxides have secondary and/or tertiary carbons adjacent to one another, but which favor termination (instead of methylation) when alkoxides contain tertiary carbons vicinal to primary carbons (Fig. 8).³¹ These desorption events (*via* H-transfer)



Scheme 2 Chain growth sequence for the homologation of dimethyl ether, including re-incorporation of alkanes *via* dehydrogenation (using adamantane as a hydrogen transfer co-catalyst). HT, Me, Is, and C labels represent hydrogen transfer, methylation, isomerization, and cracking reactions, respectively. 'CH₂' represents surface methylating species derived from dimethyl ether. Reprinted from ref. 32 with permission from Elsevier.

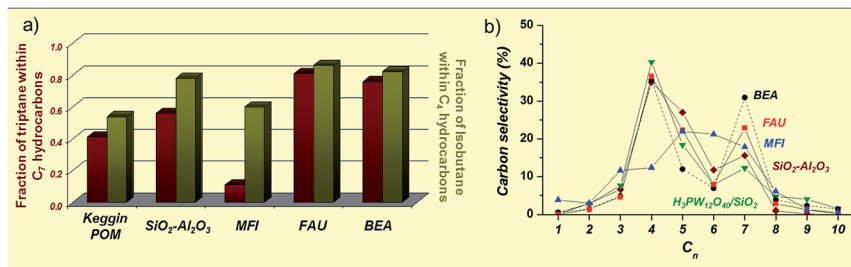


Fig. 7 (a) Selectivities to triptane within C₇ products (red bars) and isobutane within C₄ products (green bars) for dimethyl ether homologation at 473 K on zeolites (BEA, FAU, MFI) and amorphous solid acids (5 wt% H₃PW₁₂O₄₀/SiO₂ and SiO₂-Al₂O₃). (b) Product selectivities (carbon basis) for DME homologation at 473 K on BEA (●), FAU (■), MFI (▲), 5 wt% H₃PW₁₂O₄₀/SiO₂ (▼), and SiO₂-Al₂O₃ (◆). Reprinted from ref. 33 with permission from Elsevier.

involve transition states that cannot readily form in 10-MR zeolites (*e.g.* MFI), which must therefore desorb fragments of alkoxide intermediates as alkenes *via* β-scission in order to complete catalytic turnovers. Therefore, such 10-MR aluminosilicates, which are typically used in C₁ homologation processes at higher temperatures,²⁴ cannot form products with the skeleton structure and size dictated by the undisturbed carbenium ion chemistry that preferentially forms isobutane and triptane. In contrast, hydrogen transfer readily occurs, often facilitated by confinement within voids, on aluminosilicates with 12-MR voids and channels (FAU, BEA) or mesoporous networks (amorphous SiO₂-Al₂O₃); such unique selectivities are evident for both stronger acids (phosphotungstic Keggin polyoxometalates dispersed on SiO₂) and for the significantly weaker aluminosilicate acids (Fig. 7).³³

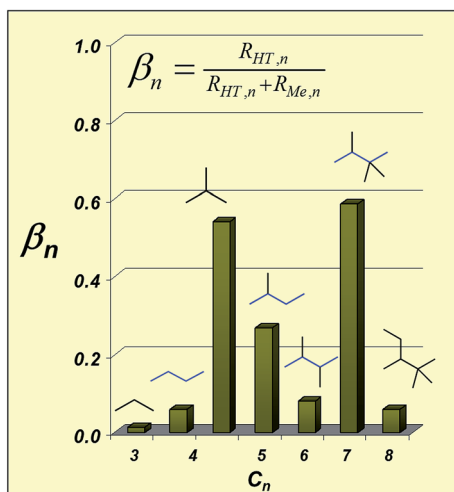


Fig. 8 Termination probabilities (β ; defined as the ratio of the rate of hydrogen transfer to the sum of the rates of hydrogen transfer and methylation) of molecules formed along the chain growth path to triptane.³¹

Competitive reactions between ^{13}C -labeled DME and unlabeled alkenes were used to measure the rates and selectivities of methylative growth and of H-transfer for alkene-derived alkoxides of specific chain length and backbone.³¹ These studies demonstrated that C_1 -species add to alkoxides at locations that retain a four-carbon backbone, because such routes avoid cyclic transition states with primary carbenium-ion character. The specific isomers formed *via* methylation exhibit much lower rates for skeletal isomerization (and β -scission) than for H-transfer or subsequent methylation, thus mitigating backbone disruptions along the path to triptane (Fig. 9 and 10). Less frequent isomerization events (and infrequent methylation at other positions) form backbones that deviate from the four-carbon chain required for triptane formation. These species, however, rapidly grow to C_{8+} hydrocarbons because isomers that lack the four-carbon backbone form alkoxides with secondary-tertiary structures that prefer to methylate instead of terminating *via* hydrogen transfer (Fig. 10). Chain termination probabilities (β_n , defined in Fig. 8) reached a maximum value for triptyl species and high values for *tert*-butoxides. The C_8 species resulting from methylation of triptane (and other C_7 isomers) exhibit very low β values (Fig. 8), because they undergo facile β -scission to form *tert*-butoxides that desorb *via* rapid H-transfer to form isobutane. Thus, any chain growth “mistakes” along the path to triptyl backbones are resolved kinetically *via* the formation of isobutane, which, as we show below, can be re-inserted into the methylation cycle *via* its own involvement in H-transfer. Such pathways lead to chains that preferentially terminate as triptane and isobutane because tertiary carbenium ions that mediate hydrogen

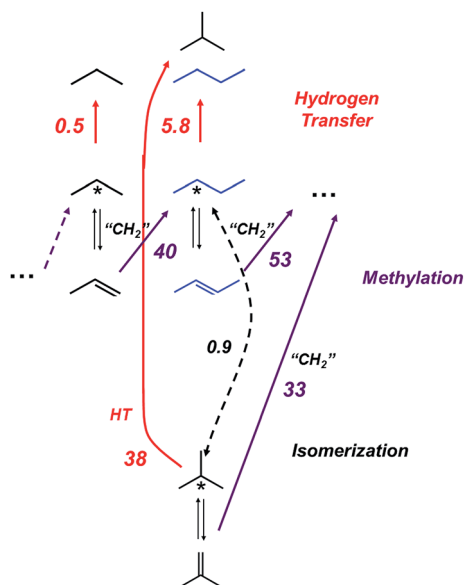


Fig. 9 Rates ($\mu\text{mol} [\text{mol}_{\text{Al}} \text{s}]^{-1}$) of methylation, hydrogen transfer, and skeletal isomerization for C_3 and C_4 species formed during homologation reactions of dimethyl ether at low temperatures. Rates were determined from co-reactions of ^{13}C -labeled dimethyl ether (78 kPa) and unlabeled propene, *trans*-2-butene, or isobutene (0.5 kPa) at 473 K on H-BEA ($\text{Si}/\text{Al} = 12.5$).³¹

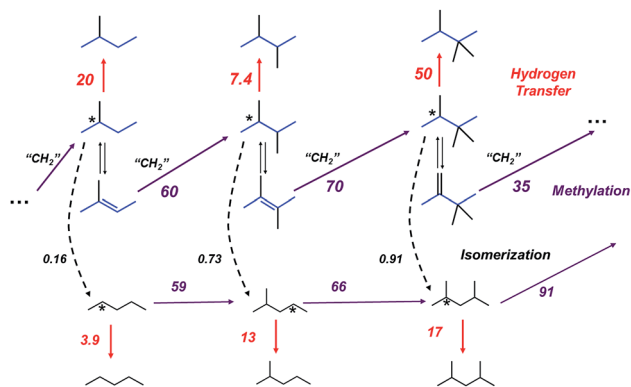


Fig. 10 Rates ($\mu\text{mol} [\text{mol}_{\text{Al}} \text{s}]^{-1}$) of methylation, hydrogen transfer, and skeletal isomerization for C_5 – C_7 species formed during homologation reactions of dimethyl ether at low temperatures. Rates were determined from co-reactions of ^{13}C -labeled dimethyl ether (78 kPa) and unlabeled 2-methyl-2-butene, 2-pentene, 2,3-dimethyl-2-butene, 2-methyl-2-pentene, triptene, or 2,4-dimethyl-2-pentene (0.5 kPa) at 473 K on H-BEA ($\text{Si}/\text{Al} = 12.5$).³¹

transfer in triptyl and isobutyl species are much more stable than the primary carbenium ions required for their respective methylation reactions.

The stoichiometry of DME or CH_3OH homologation reactions leads to the formation of alkanes that contain more H-atoms than those remaining after oxygen rejection as H_2O from DME (or CH_3OH), thus requiring the stoichiometric formation of unsaturated co-products, predominantly hexamethylbenzene (Scheme 2). The methylative homologation of alkanes with DME/ CH_3OH leads to the orderly addition of methyl groups to an alkane-derived alkoxide to form larger alkanes, without requiring any addition or rejection of H-atoms.³² The incorporation of added alkanes into C_1 -homologation chains occurs on all solid acids, as shown by the reactions of unlabeled alkanes with different backbones to ^{13}C -labeled DME, which lead to the alkane-derived ^{12}C fractions shown in Fig. 11 for H-BEA. Such alkanes form alkoxides *via* a concerted H-transfer step to growing alkoxide chains, thus enabling alkoxide desorption as alkanes.

The presence of H-donor alkanes containing tertiary C–H bonds leads to higher rates of H-transfer, and the rates of H-transfer (from all H-donors) are markedly enhanced by using adamantane, which acts as a hydride transfer co-catalyst (Fig. 11). Adamantane dissects the H-transfer process, which typically occurs *via* the concerted transfer from a donor to an acceptor, into two separate steps: H-transfer from adamantane to alkoxides (to give an alkane and an adamantyl cation) and then from alkanes to adamantyl cations (to re-form adamantane and a new alkane-derived alkoxide). These sequential H-transfer steps mediated by adamantane lead to lower barriers than the concerted direct transfer because of the involvement of particularly stable tertiary adamantyl cations in each of the sequential H-transfer steps. Such methylative homologation routes allow the upgrading of light alkanes to highly-branched larger alkanes, the return of isobutane formed through the kinetic resolution of over-methylation mistakes in DME homologation cycles, and the substantial elimination of the hexamethylbenzene stoichiometric requirements.

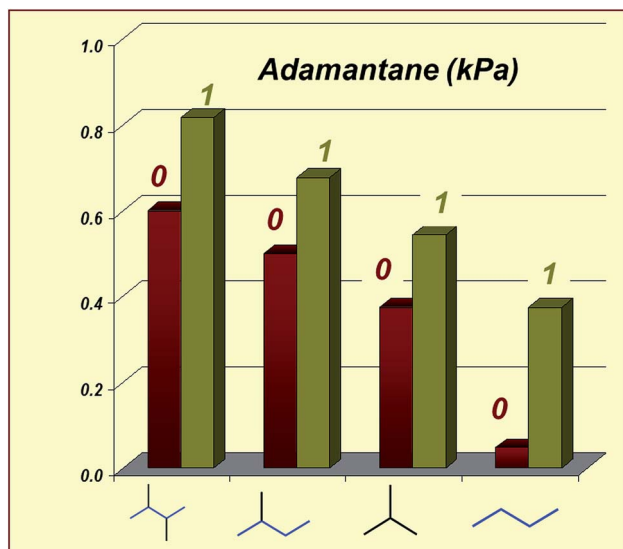


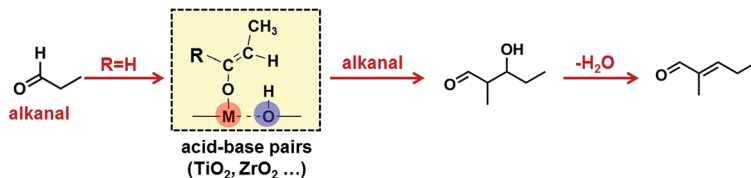
Fig. 11 Fraction of ^{12}C -atoms in triptane products from co-reaction of ^{13}C -labeled dimethyl ether with unlabeled alkanes (2,3-dimethylbutane, isopentane, isobutane, or *n*-butane) at 473 K on H-BEA in the presence (green bars) and absence (red bars) of adamantane hydride transfer co-catalysts (1 kPa).

3. Catalysis for oxygen removal and chain growth reactions of oxygenates: elementary steps and site requirements in aldol condensation, ketonization, and Prins condensation on acid–base site pairs and Brønsted acid sites at oxide surfaces

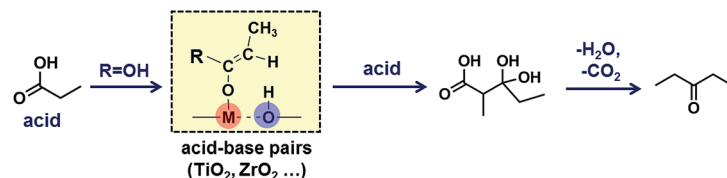
The examples discussed in this section address reactions of oxygenates through which we seek to increase their energy density *via* O-removal as H_2O or CO_2 , while preventing the consequent increase in volatility through the concurrent formation of new C–C bonds. The specific reactions of emphasis are known as aldol condensation,^{34–37} ketonization,^{38–40} and Prins condensation;^{41–43} they are depicted along with some mechanistic details in Scheme 3 and discussed here in the context of conceptual frameworks that we have chosen in order to tackle practical hurdles in controlling reactivity, selectivity, or stability on oxide catalysts that represent the state-of-the-art for these transformations.

In the studies cited above, aldol condensations involve reactions of mixtures of alkanols and alkanals (or alkanones) formed *via* the equilibration of alkanol/ H_2 feeds on the hydrogenation–dehydrogenation Cu function present as a physical mixture with the oxide-based condensation and esterification catalysts. The carbonyl compounds in these mixtures form enolate intermediates *via* C–H activation at the α -position to their C=O group (Section 3.1). Subsequent nucleophilic attack at the electrophilic C-atom in another carbonyl molecule

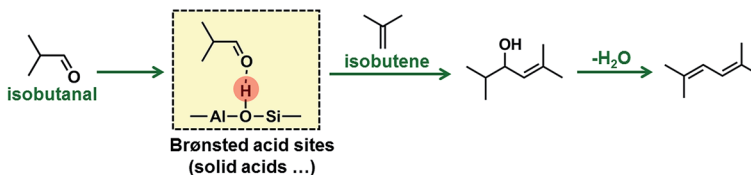
(1) Aldol condensation of carbonyl compounds



(2) Ketonization of carboxylic acids



(3) Prins condensation of alkanals and alkenes



Scheme 3 C–C coupling reactions for oxygenates on Lewis acid–base pairs of metal oxides and on Brønsted acid sites of solid acids.

leads to the formation of aldol species that subsequently dehydrate to α,β -unsaturated molecules and ultimately hydrogenate to equilibrated alkanal/alkanone/alkanol mixtures. Ketonization, in contrast, involves reactions of carboxylic acids through α -C–H activation to form 1-hydroxy-enolates that nucleophilically attack the electrophilic C-atom in another acid to form 3,3-dihydroxy-carboxylic acids, *via* steps reminiscent of those involved in aldol condensations (Section 3.2). The 3,3-dihydroxy-carboxylic acids that form from 1-hydroxy-enolates are unstable; they undergo facile dehydration and decarboxylation to form alkanones, with the loss of one C-atom from the two carboxylic acid reactants (Section 3.2). Prins condensations involve nucleophilic attack by the terminal C-atom in the C=C bond in alkenes at the electrophilic carbonyl C-atom in alkanals to form α,β -unsaturated alkanols (Section 3.3); subsequent dehydration of the α,β -unsaturated alkanols forms dienes with specific skeletal structures unattainable in other C–C formation reactions (*e.g.* alkene oligomerization^{44,45} and aldol condensation of carbonyl compounds^{35–37}).

All three types of reactions achieve the intended loss of O-atoms and a concomitant increase in product molecular weight and lead to the formation of distinct skeletal structures in products. The loss of oxygen and the increase in molecular weight are evident from the data shown in Fig. 12 for reactions of equilibrated alkanal/alkanone/alkanol mixtures on anatase TiO_2 catalysts used as physical mixtures with Cu/SiO_2 co-catalysts. The O/C ratio in the reactor effluent decreases (Fig. 12a) and its average molecular weight increases (Fig. 12b) as the conversion of the equilibrated pool increases with increasing reactor residence time as a result of condensation and esterification events.

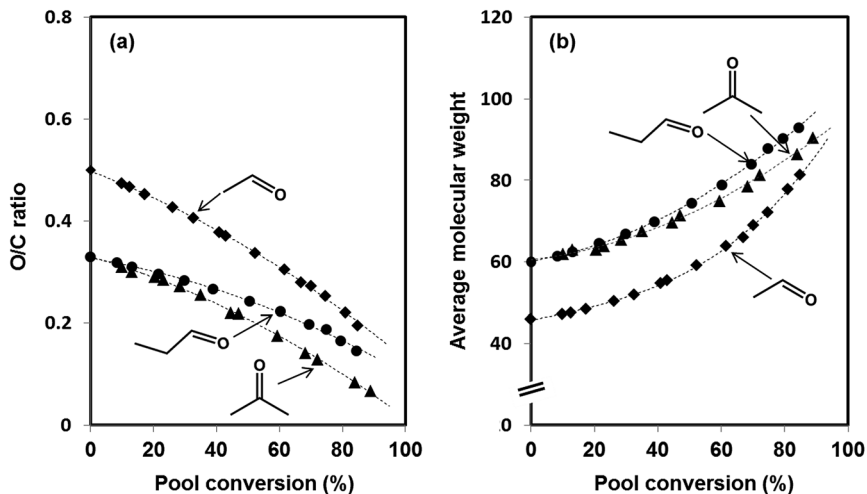


Fig. 12 (a) O/C ratio and (b) average molecular weight of the molecules in the reactor effluent as a function of alkanol-alkanal (alkanone) pool conversion (varied through changes in residence time) for acetaldehyde (\blacklozenge), propanal (\bullet) and acetone (\blacktriangle) reactants formed *in situ* from the respective alkanol ($\text{TiO}_2(\text{P}25) + 20\% \text{ wt Cu/SiO}_2$ (1 : 1 mass), 523 K, 0.8 kPa ethanol, 1-propanol, or 2-propanol, 40 kPa H_2).^{36,37} Dashed curves indicate trends.

These catalytic chemistries and the prevailing reactivity, selectivity, and catalyst stability hurdles that have obstructed their deployment in large-scale practice are addressed here through several strategies. These strategies are the result of mechanistic inquiries about the identity and kinetic relevance of plausible intermediates and elementary steps, the role of binding and confinement effects on the stability of the relevant transition states, and the kinetic coupling made possible by the presence of acid-base site pairs and a hydrogenation-dehydrogenation function within molecular diffusion distances. These strategies exploit:

(i) The scavenging of intermediates that lead to losses in yield or in available active sites through kinetic cascades in which a metal function catalyzes hydrogenation-dehydrogenation events and acid-base pairs promote C-C bond formation and deoxygenation from alkanal/alkanone/alkanol mixtures (aldol condensation, Section 3.1) or from carboxylic acids (ketonization, Section 3.2);

(ii) The stabilization of C-C bond formation transition states *via* concerted interactions with acid-base pairs at metal oxide surfaces; these concepts are based on the early studies of Tanabe about bond-making and bond-breaking at metal-oxygen (M-O) sites exhibiting moderate acid and base strength^{46,47} (Sections 3.1 and 3.2); such balanced properties lead to high condensation turnover rates and selectivities without requiring strong basic sites that are inhibited by the H_2O and CO_2 molecules formed as condensation by-products;

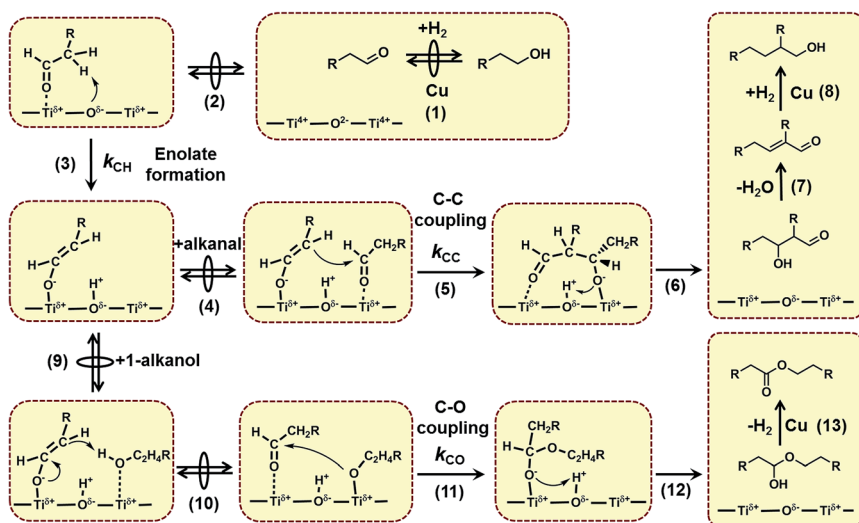
(iii) The inherent and previously unrecognized mechanistic connections between condensation and ketonization reactions, involving common enolate-like intermediates, the required Ti-O and Zr-O acid-base pairs of balanced and moderate strength, and the need to scavenge unreactive intermediates (unsaturated alkanals and alkanones in aldol condensation and bidentate carboxylates in ketonization) through bifunctional cascade strategies (Sections 3.1 and 3.2);

(iv) The preferential stabilization of alkene–alkanal Prins condensation transition states on weaker Brønsted acids over those that mediate alkene oligomerization because their smaller charge decreases the enthalpic penalty to form the conjugate anion, thus dampening the effects of acid strength, as well as the reactivity enhancements brought forth by confinement of transition states within inorganic voids of molecular dimensions, which stabilize the two transition states to the same extent because of their similar size (Section 3.3).

In all three types of reactions, a seamless connection between theory and experiment is made possible by accurate site counts, by reactivity and activation free energy comparisons based on turnover rates, by the evidence for mechanistic proposals gathered from spectroscopic and isotopic methods, and by the use of theoretical methods that rigorously account for van der Waals interactions and of structural models that consider the complex but known structures of the acid–base pairs and the Brønsted acid sites that catalyze these reactions.

3.1. Aldol condensation and esterification of oxygenate reactants mediated by concerted H-abstraction transition states on acid–base pairs of intermediate strength

Aldol condensations of alkanals and alkanones form new C–C bonds and remove O-atoms *via* activation of α -C–H bonds (step 3, Scheme 4), nucleophilic attack of carbonyls by enolates (step 5, Scheme 4), and dehydration of aldols to α,β -unsaturated carbonyl compounds (step 7, Scheme 4). These reactions lead to the decrease in O-content and an increase in product molecular weight evident from the data in Fig. 12. Oxides, such as TiO_2 and ZrO_2 , catalyze such reactions, but their unfavorable thermodynamics limit rates and favor the accumulation of unsaturated intermediates that lead to loss of selectivity *via* subsequent chain



Scheme 4 Aldol condensation and esterification pathways for C_2 – C_5 alkanol–alkanal reactants ($\text{CH}_2\text{RCH}_2\text{OH}$ – CH_2RCHO , $\text{R} = \text{H}$ or alkyl) on bifunctional $\text{TiO}_2 + \text{Cu/SiO}_2$ mixtures.^{36,37} Quasi-equilibrated steps are noted by a circle over double arrows. Reaction numbers used throughout the text are in parentheses.

growth and the formation of residues that block active sites and lead to fast deactivation.⁴⁸

A metal function, such as Cu, Pt, or Pd, even as physical mixtures with metal oxides, and the presence of H₂ leads to the facile hydrogenation of these unsaturated products and intermediates (step 8, Scheme 4), thus removing thermodynamic bottlenecks and preventing side reactions and the otherwise prevalent loss of selectivity and active sites. Such a metal function also rapidly interconverts alkanols and their dehydrogenation products (alkanals, alkanones), rendering all such species equivalent as condensation (and esterification) reactants (step 1, Scheme 4). The use of equilibrated 1-alkanol-alkanal mixtures and of a metal function also leads to esterification turnovers, made possible *via* the dehydrogenation of hemiacetals (step 13, Scheme 4) formed as unstable initial products of C–O bond formation in esterification, *via* reactions between 1-alkanols and alkanal-derived enolates (steps 9–12, Scheme 4).

Kinetic, isotopic, and theoretical assessments of the aldol condensation and esterification rates and of the mechanism of C₂–C₅ alkanols on bifunctional anatase TiO₂ mixtures with Cu/SiO₂^{36,37} have shown that the formation of enolates from alkanals/alkanones (step 3, Scheme 4) is the sole kinetically-relevant step for all reactants, consistent with measured and DFT-derived H/D kinetic isotope effects (2.3 and 2.4, respectively, ethanal-d₆, 523 K) and with the similar activation free energies obtained from theory and experiment. The C–C bonds form *via* subsequent coupling of enolates with alkanals or alkanones with the elimination of H₂O to give the α,β -unsaturated carbonyl products (steps 5–7, Scheme 4). New C–O bonds can also form from reactions of alkanal-derived enolates with 1-alkanols, a step that proceeds *via* sequential H-transfer and alkanal-alkoxide coupling steps to form unstable hemiacetals (steps 10–12, Scheme 4). The formation of C–O and C–C bonds (steps 5 and 11, Scheme 4) from a common enolate precursor determines the fate of the latter species, but not their formation rates, and thus the esterification/condensation rate ratios. Neither step (C–C or C–O bond formation) is limited by reactions involving C–H or O–H bonds, in agreement with the small measured (1.4) and DFT-derived (1.2) kinetic isotope effects (ethanol-d₆, 523 K).

Site titration experiments during acetone condensation demonstrated the involvement of acid–base pairs of intermediate strength on both TiO₂ and ZrO₂. On anatase TiO₂, enolate formation rates were unaffected by CO₂ and reversibly inhibited by pyridine and propanoic acid titrants (Fig. 13),³⁶ consistent with concerted involvement of both centers in Ti–O pairs with balanced acid and base strength. The use of propanoic acid as a strongly-bound titrant during alkanal or alkanone reactions allowed direct measurements of the number of site pairs; these numbers (3.7 nm⁻²) are consistent with the atomic density of low-index anatase surfaces and with the kinetic irrelevance of any minority defect sites, often invoked to account for the reactive properties of TiO₂ surfaces. Such site counts allowed rates to be expressed as turnover rates and measured activation free energies, allowing the accurate benchmarking of measured and DFT-derived activation free energies.

The DFT-derived activation free energies ($\Delta G_{\text{CH}}^\ddagger$) for enolate formation from C₂–C₅ oxygenates are in excellent agreement with the measured values (Fig. 14a), as is also the case for the difference in free energies between the esterification and condensation branching reactions from a given enolate ($\Delta G_{\text{CO-CC}}^\ddagger$, Fig. 14b). The

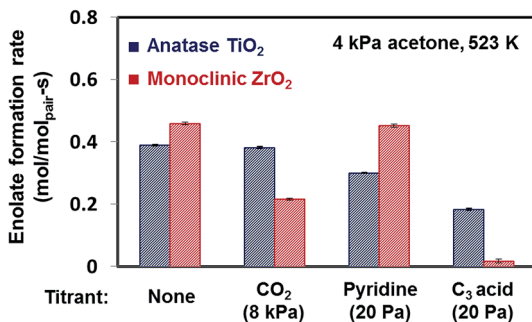


Fig. 13 Effects of CO₂, pyridine, and propanoic acid introductions on enolate formation rates of acetone on anatase TiO₂ and monoclinic ZrO₂ (oxide + 20% wt Cu/SiO₂ (1 : 1 mass), 523 K, 4 kPa acetone, 4 kPa CO₂, 20 Pa pyridine, 20 Pa propanoic acid, 40 kPa H₂).^{36,37}

stronger α -C-H bonds in alkanones lead to lower reactivity (higher $\Delta G_{\text{CH}}^\ddagger$) than for alkanals, while longer and more branched alkyls at the α -C position cause steric hindrance and higher $\Delta G_{\text{CH}}^\ddagger$ values for enolate formation (Fig. 14a). DFT-derived free energy differences between C-O and C-C bond coupling transition states ($\Delta G_{\text{CO-CC}}^\ddagger$) also agree with the measured values (Fig. 14b), indicating that alkyl substitution effects are stronger for condensation than esterification transition states (steps 5 and 11, Scheme 4). This reflects their requirement for more precise orbital alignment and the enforcement of such alignment at locations more proximate to the alkyl attachment point for condensation than for esterification transition states.³⁷

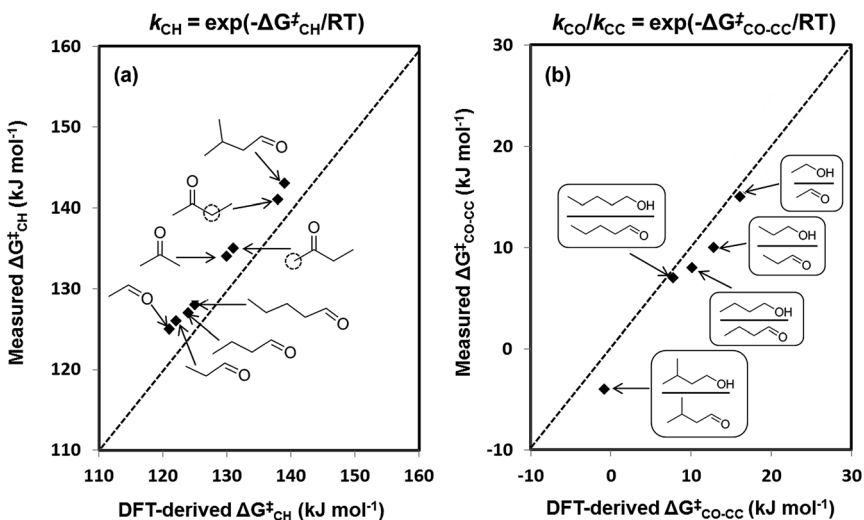


Fig. 14 Measured and DFT-derived (a) $\Delta G_{\text{CH}}^\ddagger$ and (b) $\Delta G_{\text{CO-CC}}^\ddagger$ for C₂-C₅ alkanals and alkanones on anatase TiO₂ surfaces (Ti_{5c}-O_{3c}-Ti_{5c} structures of an anatase Ti₅O₁₉H₁₈ cluster used as an acid-base pair model,³⁶ B3LYP + D3BJ, 6-311G(d,p) for C, H, and O atoms, LANL2DZ for Ti atoms; 523 K, 1 bar). Dashed lines represent the parity lines. Adapted with permission from ref. 37. Copyright 2016 American Chemical Society.

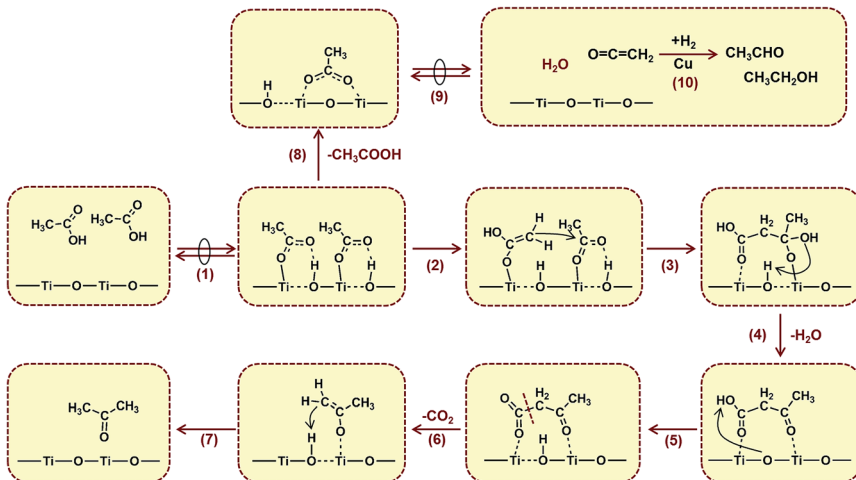
These mechanistic conclusions and their consequences for reactivity and selectivity apply to a broad range of oxygenate reactants and remain unchanged on Zr–O pairs at monoclinic ZrO₂ surfaces, which exhibit enolate formation turnover rates (Fig. 13), activation free energies, and isotope effects similar to those on anatase TiO₂.³⁷ Enolate formation rates on monoclinic ZrO₂ were reversibly inhibited by CO₂, but not by pyridine (Fig. 13), because acid–base pairs on monoclinic ZrO₂ contain stronger basic sites and weaker acid sites than anatase TiO₂. Yet, such site pairs provide the balance of acid–base strength required to stabilize the concerted α -C–H bond activation transition states that mediate enolate formation. These conclusions are consistent with DFT-derived interaction energies of H⁺ and OH[−] (as probes of the strength of acid and basic sites) on site pairs prevalent on low-index surfaces of ZrO₂ and TiO₂.³⁷

3.2. Ketonization of carboxylic acids mediated by C–C coupling transition states on acid–base pairs of intermediate strength

The replacement of a H-atom at the carbonyl C-atom in alkanals by an OH group to give carboxylic acids transforms their C–C bond formation chemistries from aldol condensation into ketonization routes. Ketonization converts carboxylic acids into equimolar mixtures of alkanones, CO₂, and H₂O, while forming a new C–C bond and removing three of the four O-atoms in the two acid reactants (Scheme 3(2)). As in the case of aldol condensation (Section 3.1), ketonization requires the cleavage of the α -C–H bond in one of the acid reactants before the formation of the new C–C bond at the activated C-atom *via* reaction with another acid molecule. These reactions are catalyzed by metal oxides, such as TiO₂ and ZrO₂, which also catalyze aldol condensations, suggestive of a mechanistic link between these two types of chemical transformations.

The demonstrated involvement of enolates in aldol condensation on TiO₂ and ZrO₂ (Section 3.1) makes it plausible that similar enolate-like species (1-hydroxy-enolates) are also involved in ketonization catalytic sequences (step 2, Scheme 5). These species would then participate in nucleophilic attack with another acid to form 3,3-dihydroxy-carboxylic acids with the new C–C bond (step 3, Scheme 5). Such molecules readily decompose *via* dehydration and decarboxylation reactions to form alkanones (steps 4–6, Scheme 5), in contrast with the H₂O elimination step that forms condensation products from aldols without the loss of a C-atom (step 7, Scheme 4). These similarities in mechanisms and the common involvement of Lewis acid–base pairs, supported by theoretical treatments,⁴⁰ allow us to extend the use of the titration methods developed to measure the number of active sites during aldol condensation reactions to their ketonization counterparts.^{36,37}

Acetic acid ketonization turnover rates (1.0 kPa; 523 K) are slightly higher on monoclinic ZrO₂ (0.51 ks^{−1}, Fig. 15) than on tetragonal ZrO₂ or anatase TiO₂ (0.44 and 0.25 ks^{−1}), but much lower on rutile TiO₂ (0.024 ks^{−1}). These reactivity trends are observed in parallel with deactivation rate constants that are larger on the more active oxides (Fig. 15). Infrared spectra during ketonization on anatase TiO₂⁴⁰ show that bidentate acetates (*AcO*), bound to two vicinal Ti–O pairs with their two O-atoms each interacting with one Ti center and the dissociated proton bound onto an O site, form *via* slow dissociation on acid–base pairs (step 8, Scheme 5) and act as unreactive spectator species during steady-state catalysis. Cu co-catalysts, present as physical mixtures with these oxides and added H₂



Scheme 5 Ketonization pathway for acetic acid on bifunctional $\text{TiO}_2 + \text{Cu/SiO}_2$ mixtures. Quasi-equilibrated steps are noted by a circle over double arrows. Reaction numbers used throughout the text are in parentheses.

markedly decreased deactivation rates and led to higher steady-state ketonization rates.⁴⁰ These protecting effects reflect the scavenging of ketene, present at trace concentrations *via* adsorption–desorption equilibrium with $^*\text{AcO}^*$ (step 9, Scheme 5), to form acetaldehyde and ethanol (step 10, Scheme 5), thus providing a route to lower steady-state coverages of unreactive $^*\text{AcO}^*$ and thus lower deactivation rates during ketonization.

Combined kinetic, spectroscopic, and DFT assessments of reactions of $\text{C}_2\text{--C}_4$ carboxylic acids on anatase TiO_2 ⁴⁰ have shown that monodentate carboxylates, the reactive intermediates in 1-hydroxy-enolate formation (step 2, Scheme 5), bind strongly at Ti–O pairs *via* concerted interactions of its two carbonyl O-atoms with the Ti center and the abstracted H-atom (bound at the basic O-atom in the site pair) (e.g. AcO^* for acetic acid; step 1, Scheme 5); such binding properties lead to

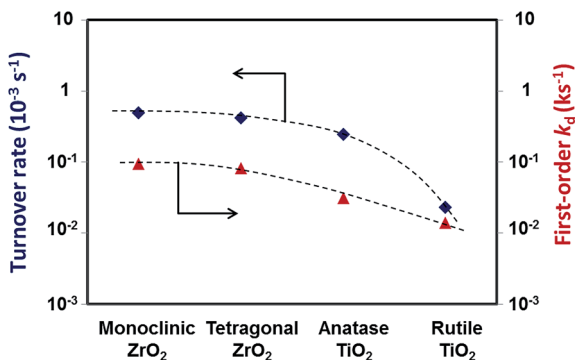
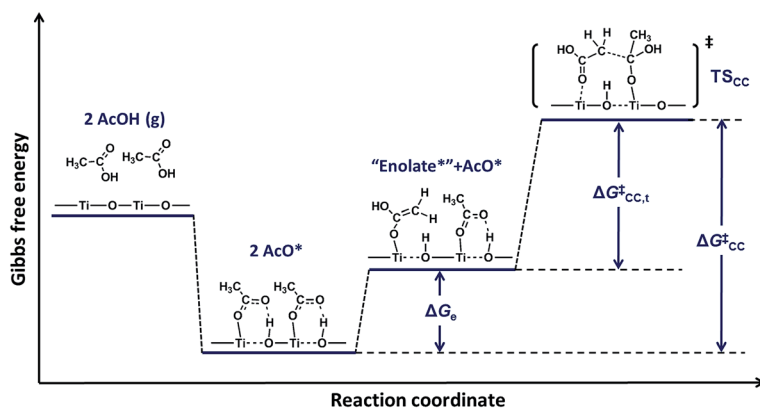


Fig. 15 Turnover rates and first-order deactivation constants (k_d) for acetic acid ketonization on TiO_2 and ZrO_2 catalysts (523 K, 1.0 kPa acetic acid).⁴⁰ Dashed lines indicate trends.

densely-covered surfaces at all practical ketonization conditions. The weak measured H/D kinetic isotope effects (acetic acid- d_4 , 1.1, 523 K) and the nearly saturated monolayers of monodentate carboxylates evident in infrared spectra during catalysis, indicate that the nucleophilic attack of co-adsorbed acids by 1-hydroxy-enolates (step 3, Scheme 5) is the sole kinetically-relevant step in ketonization catalytic cycles. These conclusions are consistent with measured kinetic effects of acid pressure, with the effects of alkyl substituents on ketonization turnover rates, and with DFT-derived activation free energy barriers using periodic slab models.⁴⁰

Ketonization rates of C_2 – C_4 carboxylic acids on anatase TiO_2 become independent of acid pressures even at pressures (~ 1 kPa) well below those typical of catalytic practice (>0.1 MPa). These data indicate that ketonization occurs on oxide surfaces nearly saturated with monodentate carboxylate intermediates.⁴⁰ Zero-order ketonization turnover rates reflect free energy differences (ΔG_{CC}^\ddagger) between the C–C coupling transition state and two monodentate carboxylate species (Scheme 6). Acetic acid turnover rates on monoclinic ZrO_2 give ΔG_{CC}^\ddagger values that are smaller than on anatase TiO_2 (136 vs. 166 kJ mol^{-1} , 523 K, 0.1 MPa acetic acid⁴⁰), consistent with DFT-derived values on the low-index exposed surfaces of these oxides (140 vs. 160 kJ mol^{-1}). These ΔG_{CC}^\ddagger differences, indicative of the stability of the C–C bond formation transition state relative to the monodentate carboxylate precursors, show that ketonization reactions are favored on monoclinic ZrO_2 surfaces over anatase TiO_2 surfaces. In contrast, aldol condensation turnover rates, which reflect the stability of the enolate formation transition state relative to a gaseous carbonyl reactant, are similar on the acid–base site pairs present on these two surfaces (Section 3.1). The different consequences of the properties of acid–base site pairs for these two reactions reflect the specific roles of the Lewis acid and base centers on their respective transition states and precursors, as discussed next.



Scheme 6 Schematic reaction coordinate diagram for ketonization of acetic acid on anatase TiO_2 . ΔG_{CC}^\ddagger represents the experimentally accessible apparent free energy barrier for the C–C bond formation, and equals to the sum of the free energy difference between a bound 1-hydroxyl-enolate and a monodentate carboxylate (ΔG_e) and the free energy difference between the C–C coupling transition state and its 1-hydroxyl-enolate–carboxylate pair precursor ($\Delta G_{CC,t}^\ddagger$).

Ketonization activation free energy (ΔG_{CC}^\ddagger) differences between Zr–O and Ti–O pairs can reflect differences in either the free energy of formation of 1-hydroxy-enolates from AcO^* on M–O site pairs (M = Ti, Zr; ΔG_e , Scheme 6) or that of the formation of the C–C coupling transition state from its 1-hydroxy-enolate– AcO^* precursors ($\Delta G_{CC,t}^\ddagger$, Scheme 6). Their relative contributions depend on the coverages and reactivity of the 1-hydroxy-enolates in forming the C–C bond with a vicinal AcO^* . DFT treatments show that monoclinic ZrO_2 surfaces are more reactive than those of anatase TiO_2 because they form higher 1-hydroxy-enolate concentrations at Zr centers (ΔG_e : 44 vs. 111 kJ mol^{-1} for monoclinic ZrO_2 and anatase TiO_2), as a consequence of stronger basicity,³⁷ which disfavors the reprotonation of 1-hydroxy-enolates to form AcO^* .³⁸ In contrast, the activation of α -C–H bonds in carbonyl compounds to form enolates on acid–base pairs involves concerted transition states. In such structures, the α -H-atom is abstracted by the basic O site and the incipiently-formed enolate moiety is stabilized by a Lewis acid center. The stronger basic sites on ZrO_2 (relative to TiO_2) compensate for the weaker Zr centers in the concerted stabilization of enolate moieties, leading to the similar observed condensation reactivity of TiO_2 and ZrO_2 surfaces.

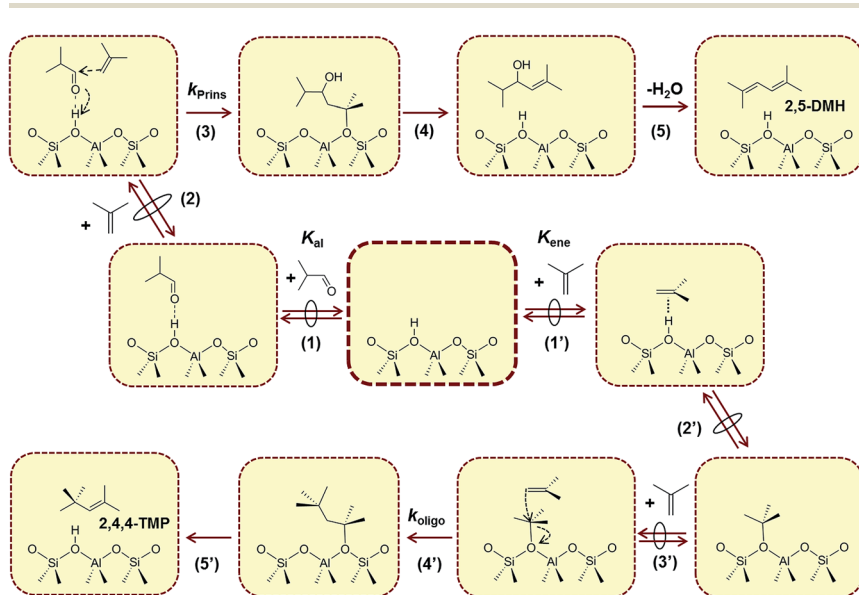
Alcohol condensation and ketonization both require acid–base pairs and involve nucleophilic attack of enolate-like species at the carbonyl C-atom of another molecule to form a C–C bond. The weak adsorption of alkanals and alkanones leads to acid–base pairs that remain essentially uncovered during condensation turnovers; as a result such turnovers are limited by enolate formation. The dissociation of carboxylic acids, in contrast, forms strongly-bound monodentate carboxylates, which saturate surfaces at all conditions of ketonization catalysis. Ketone turnovers become limited by C–C coupling of (carboxylate-derived) 1-hydroxy-enolates with another acid on such surfaces. The acid–base balance required for enolate formation and the stronger basic moieties that increase enolate coverages during ketonization illustrate how catalytic sequences, intrinsically connected *via* analogous elementary rearrangements, lead to different acid–base requirements as a result of the identity of the kinetically-relevant step.

3.3. Alkanal–alkene Prins condensation mediated by C–C coupling transition states on Brønsted solid acids: effects of acid strength and of confinement within voids of molecular size

The activation of alkanals (or alkanones) and carboxylic acids on acid–base site pairs forms enolate-like species that act as strong nucleophiles in the subsequent formation of a new C–C bond (Sections 3.1 and 3.2). In contrast, protonation of carbonyl compounds on Brønsted acids renders these species strongly electrophilic, leading to their facile ability to react even with weak nucleophiles, such as alkenes, to form new C–C bonds. These latter routes are discussed in this section in the context of alkanal–alkene Prins condensation reactions. Prins condensations form C–C bonds between the carbonyl C-atoms in alkanals and the terminal C-atoms at $\text{C}=\text{C}$ bonds in alkenes, with the concurrent removal of O-atoms *via* dehydration steps that convert the α,β -unsaturated alkanol formed to dienes (Scheme 3(3)). Specifically, isobutanal–isobutene reactions selectively form 2,5-dimethyl-hexadiene regioisomers (2,5-DMH); their skeletal structures render such species convenient as precursors to *p*-xylene from isobutene and isobutanal co-reactants that can be derived from isobutanol, a product of biomass fermentations.⁴²

Isobutanal–isobutene Prins condensation occurs on solid acids, in parallel with isobutene oligomerization to 2,4,4-trimethyl-pentene regioisomers (2,4,4-TMP; steps 1'–5', Scheme 7) and with secondary isomerization, cyclization, and β -scission of 2,5-DMH primary condensation products. Non-coordinating 2,6-di-*tert*-butylpyridine titrants fully suppressed reactivity for Prins condensation and oligomerization on all acids;⁴³ thus, both reactions occur exclusively on Brønsted acid sites, without contributions from Lewis acids or acid–base site pairs. Turnover rates (per proton) for Prins condensation (r_{Prins}) and oligomerization (r_{oligo}) both increased as the strength of the acid sites increased from amorphous aluminosilicates to niobic acid and heteropolytungstic acids ($\text{H}_3\text{PW}_{12}\text{O}_{40}$) (Fig. 16), but $r_{\text{Prins}}/r_{\text{oligo}}$ ratios were significantly higher on the weaker acids (Fig. 16). Kinetic data and theoretical treatments indicate that isobutanal–isobutene Prins condensation rates are limited by C–C bond formation between a H-bonded isobutanal and a gaseous isobutene molecule (step 3, Scheme 7); parallel isobutene oligomerization reactions are limited by C–C bond formation between an isobutene-derived alkoxide and a gaseous isobutene molecule (step 4', Scheme 7).

Measured second-order rate constants for Prins condensation (k_{Prins}) and oligomerization (k_{oligo}) were both smaller on Al-MCM-41 (12 ± 2 and 1.2 ± 0.3 ks^{-1} kPa^{-2} per H^+ ; 473 K) than on stronger $\text{H}_3\text{PW}_{12}\text{O}_{40}$ acids (25 ± 1 and 12 ± 1 ks^{-1} kPa^{-2} per H^+),⁴³ while $k_{\text{Prins}}/k_{\text{oligo}}$ ratios were much higher on Al-MCM-41 (10.3 ± 0.2 ; 473 K) than on $\text{H}_3\text{PW}_{12}\text{O}_{40}$ (2.0 ± 0.1). These trends are consistent with theoretical estimates based on aluminosilicate slabs and Keggin $\text{H}_3\text{PW}_{12}\text{O}_{40}$ cluster models, which confirm the lower reactivity but higher Prins selectivity of weaker acids. The C–C formation transition states for Prins condensation (TS_{Prins} ;



Scheme 7 Reaction pathways for isobutanal–isobutene Prins condensation and isobutene oligomerization on Brønsted solid acids (shown for aluminosilicates as an illustrative example). Quasi-equilibrated steps are noted by a circle with double arrows. Reaction numbers used throughout the text are in parentheses ((1–5) for Prins condensation; (1'–5') for oligomerization).

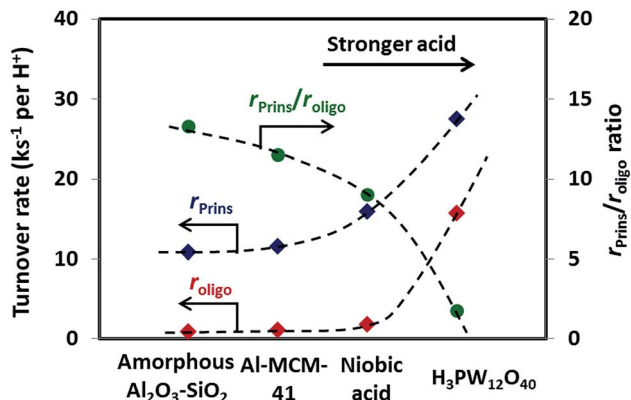


Fig. 16 Turnover rates of Prins condensation (r_{Prins}) and isobutene oligomerization (r_{Oligo}) and their rate ratios on solid acids (473 K, 2.0 kPa isobutanal, 1.0 isobutene).⁴³

step 3, Scheme 7) and oligomerization (TS_{oligo} ; step 4', Scheme 7) are positively-charged, but TS_{Prins} structures become full ion-pairs only on stronger acids, while TS_{oligo} structures are present as full ion-pairs, irrespective of acid strength. As a result, both k_{Prins} and k_{oligo} increase with acid strength, but the TS_{oligo} structure preferentially benefits from the greater stability of the conjugate anions in the stronger acids, leading to higher 2,5-DMH selectivities, reflected on the $k_{\text{Prins}}/k_{\text{oligo}}$ ratios, on weaker acids.

The TS_{Prins} and TS_{oligo} structures on aluminosilicates are similar in size (van der Waals volume 0.153 vs. 0.144 nm³) and are therefore stabilized to the same extent by van der Waals contacts with the walls of the confining voids. Consequently, their similar size and the similar acid strength of sites in aluminosilicates, irrespective of framework structure,⁴⁹ lead to similar $k_{\text{Prins}}/k_{\text{oligo}}$ ratios (15–20, 473 K) on all mesoporous and microporous aluminosilicates.⁵⁰ These TS_{Prins} and TS_{oligo} structures, however, are significantly larger than their respective precursors (H-bonded isobutanal and *tert*-butoxide, respectively), causing both r_{Prins} and r_{oligo} values to sense the size (and shape) of the confining voids. Measured first-order Prins condensation rate constants ($k_{\text{Prins}}/K_{\text{al}}$; K_{al} , isobutanal adsorption constant) reflect the Gibbs free energy of the TS_{Prins} relative to a H-bonded isobutanal and a gaseous isobutene molecule. These $k_{\text{Prins}}/K_{\text{al}}$ values increase with increasing void size (from TON to BEA to FAU, Fig. 17), but then decrease for even larger voids (Al-MCM-41), because of less effective van der Waals contacts between the transition state and the mesoporous voids. Protons at the cage-like intersections formed by MFI channels gave slightly larger $k_{\text{Prins}}/K_{\text{al}}$ values (~two-fold) than those within cylindrical channels in BEA (Fig. 17), in spite of their similar diameters, as a result of the quasi-spherical shape of MFI intersections, which provide a better fit for the geometric features of TS_{Prins} structures.

The conversion of primary 2,5-DMH products to skeletal (2,4-DMH, 3,4-DMH) or cyclic (1,4-dimethyl-cyclohexene) isomers is favored for voids of intermediate size (MFI, BEA),⁵⁰ suggesting that the required transition states are preferentially stabilized relative to TS_{Prins} . MFI structures showed a unique propensity to form 1,4-dimethyl-cyclohexene, apparently as a result of cage-channel undulations

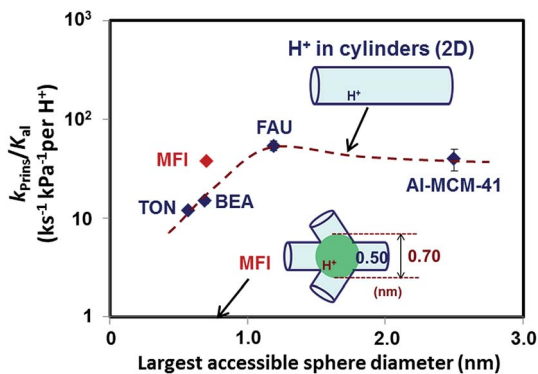


Fig. 17 Measured k_{Prins}/K_{al} values as a function of the largest accessible sphere diameter of aluminosilicate voids at 473 K.⁵⁰

along the MFI structure, which allow the formation of 2,5-DMH and its skeletal isomers at cage-like locations, but impede their egress *via* diffusion through the interconnecting apertures. Their intra-cage cyclization can form faster diffusing species (*e.g.*, 1,4-dimethyl-cyclohexene); such molecules exhibit similar cross sectional areas but much shorter lengths than the acyclic dimethyl isomers.⁵⁰

4. Conclusions

The examples discussed here represent a small subset within the theme of catalysts for fuels; they intend to illustrate the ubiquitous challenges in converting atypical carbon feedstocks, which lack the required volatility or energy density, into liquid fuels *via* the formation of new C–C bonds and the removal of excess oxygen. The formidable hurdles imposed by these requirements are addressed by the preferential stabilization of specific transition states, conferred through solvation within inorganic voids or by intrapore liquids, by acid sites or acid–base site pairs of specific acid/base strength and geometry, by the *in situ* generation of co-reactants that shift transition states along the reaction coordinate, by cascade strategies that protect active sites and circumvent thermodynamic bottlenecks, and by enforcing carbenium-ion chemistries unperturbed by side reactions. These hurdles and their intended solutions are framed here in the context of their underpinnings in chemical kinetics concepts, specifically the formalism of transition state theory, enabled by a seamless combination of kinetic, spectroscopic, isotopic, and theoretical methods. These foundational strategies transcend, in our view, the specific problems at hand, as we hope the diverse problems tackled have been able to demonstrate.

Acknowledgements

The work described here represents contributions also from Patricia Cheung and John Ahn, in addition to those of the co-authors, who also acknowledge collaborations with Jay Labinger, John Bercaw, and Glenn Sunley in the C_1 homologation and carbonylation studies. The financial support by BP, p.l.c. for all the examples shown and by the Marie Skłodowska Curie Fellowship Program, and the

Vermeulen Chair Endowment Fund at the University of California-Berkeley for the dimerization studies are acknowledged with thanks.

References

- 1 B. C. Gates, J. R. Katzer and G. C. A. Schuit, *Chemistry of Catalytic Processes*, McGraw-Hill, 1979; C. H. Bartholomew and R. J. Farrauto, *Fundamentals of Industrial Catalytic Processes*, John Wiley & Sons, 2011; J. N. Armor, *Catal. Today*, 2011, **163**, 3; C. Martinez and A. Corma, *Coord. Chem. Rev.*, 2011, **255**, 1559; W. Vermieren and J. P. Gilson, *Top. Catal.*, 2009, **52**, 1131.
- 2 A. I. Olivos-Suarez, A. Szecsenyi, E. J. M. Hensen, J. Ruiz-Martinez, E. V. Pidko and J. Gascon, *ACS Catal.*, 2016, **6**, 2695; C. Mesters, *Annu. Rev. Chem. Biomol. Eng.*, 2016, **7**, 223.
- 3 G. W. Huber, S. Iborra and A. Corma, *Chem. Rev.*, 2006, **106**, 4044; D. M. Alonso, J. Q. Bond and J. A. Dumesic, *Green Chem.*, 2010, **12**, 1493; M. A. Mellner, J. M. Gallo, D. M. Alonso and J. A. Dumesic, *ACS Catal.*, 2015, **5**, 3354; J. S. Luterbacher, D. M. Alonso and J. A. Dumesic, *Green Chem.*, 2014, **16**, 4816; G. W. Huber and A. Corma, *Angew. Chem., Int. Ed.*, 2007, **46**, 2.
- 4 J. H. Lunsford, *Catal. Today*, 2000, **63**, 165.
- 5 J. A. Labinger and K. C. Ott, *J. Phys. Chem.*, 1987, **91**, 2682; J. A. Labinger, *Catal. Lett.*, 1988, **1**, 371.
- 6 C. A. Mims, R. Mauti, A. M. Dean and K. D. Rose, *J. Phys. Chem.*, 1994, **98**, 13357; S. C. Reyes, E. Iglesia and C. P. Kelkar, *Chem. Eng. Sci.*, 1993, **48**, 2643; S. C. Reyes, C. P. Kelkar and E. Iglesia, *Catal. Lett.*, 1993, **19**, 13372.
- 7 A. Palermo, J. P. H. Vazquez, A. F. Lee, M. S. Tikhov and R. M. Lambert, *J. Catal.*, 1998, **177**, 259; S. Pak, P. Qiu and J. H. Lunsford, *J. Catal.*, 1998, **79**, 222.
- 8 K. Takanabe and E. Iglesia, *Angew. Chem., Int. Ed.*, 2008, **47**, 7689.
- 9 K. Takanabe and E. Iglesia, *J. Phys. Chem. C*, 2009, **113**, 10131.
- 10 Y. Liang, Z. Li, M. Nourdine, S. Shahid and K. Takanabe, *ChemCatChem*, 2014, **6**, 1245.
- 11 K. Takanabe and S. Shahid, *AIChE J.*, 2017, **63**, 105.
- 12 G. J. Sunley and D. J. Watson, *Catal. Today*, 2000, **58**, 293.
- 13 A. Bhan, A. Allian, G. Sunley, D. Law and E. Iglesia, *J. Am. Chem. Soc.*, 2007, **129**, 4919.
- 14 P. Cheung, A. Bhan, G. L. Sunley, D. Law and E. Iglesia, *J. Catal.*, 2007, **245**, 110.
- 15 A. Bhan and E. Iglesia, *Acc. Chem. Res.*, 2008, **41**, 559.
- 16 M. Neurock, *Ind. Eng. Chem. Res.*, 2010, **49**, 10183.
- 17 M. Boronat, C. Martinez and A. Corma, *Phys. Chem. Chem. Phys.*, 2011, **13**, 2603.
- 18 I. Agirrezabal-Telleria and E. Iglesia, *J. Catal.*, 2017, submitted.
- 19 J. C. Mol, *J. Mol. Catal. A: Chem.*, 2004, **213**, 39.
- 20 J. Canivet, S. Aguado, Y. Schuurman and D. Farrusseng, *J. Am. Chem. Soc.*, 2013, **135**, 4195.
- 21 R. D. Andrei, M. I. Popa, F. Fajula and V. Hulea, *J. Catal.*, 2015, **323**, 76.
- 22 J. Heveling, A. Van Der Beek and M. De Pender, *Appl. Catal.*, 1988, **42**, 325.
- 23 A. Lacarriere, J. Robin, D. Swierczynski, A. Finiels, F. Fajula, F. Luck and V. Hulea, *ChemSusChem*, 2012, **5**, 1787.
- 24 M. Stöcker, *Microporous Mesoporous Mater.*, 1999, **29**, 3–48; C. D. Chang and A. J. Silvestri, *J. Catal.*, 1977, **47**, 249; C. D. Chang, *Catal. Rev.: Sci. Eng.*, 1983, **25**, 1; S. Kolbe, *Acta Chem. Scand., Ser. A*, 1986, **40**, 711.

- 25 K. Amakawa, S. Wrabetz, J. Kröhnert, G. Tzolova-Müller, R. Schlögl and A. Trunschke, *J. Am. Chem. Soc.*, 2012, **134**, 11462; K. Ding, A. Gulec, A. M. Johnson, T. L. Drake, W. Wu, Y. Lin, E. Weitz, L. D. Marks and P. C. Stair, *ACS Catal.*, 2016, **6**, 5740; A. Salameh, C. Coperet, J. M. Basset, V. P. W. Bohm and M. Roper, *Adv. Synth. Catal.*, 2007, **349**, 238; S. Lwin and I. E. Wachs, *ACS Catal.*, 2014, **4**, 2505.
- 26 R. D. Andrei, M. I. Popa, F. Fajula, C. Cammarano, A. A. Khudhair, K. Bouchmella, P. H. Mutin and V. Hulea, *ACS Catal.*, 2015, **5**, 2774; L. Li, R. D. Palcheva and K. J. Jens, *Top. Catal.*, 2013, **56**, 783.
- 27 S. A. Tabak, F. J. Krambeck and W. E. Garwood, *AIChE J.*, 1986, **32**, 1526; R. J. Quann, L. A. Green, S. A. Tabak and F. J. Krambeck, *Ind. Eng. Chem. Res.*, 1988, **27**, 565; A. Corma and A. Martínez, *Catal. Rev.: Sci. Eng.*, 1993, **35**, 483; L. F. Albright, *Ind. Eng. Chem. Res.*, 2009, **48**, 1409; G. S. Nivarthi, A. Feller, K. Seshan and J. A. Lercher, *Microporous Mesoporous Mater.*, 2000, **75**, 35.
- 28 J. E. Bercaw, P. L. Diaconescu, R. H. Grubbs, R. D. Kay, S. Kitching, J. A. Labinger, X. Li, P. Mehrkhodavandi, G. E. Morris, G. J. Sunley and P. Vagner, *J. Org. Chem.*, 2006, **71**, 8907; J. E. Bercaw, P. L. Diaconescu, R. H. Grubbs, N. Hazari, R. D. Kay, J. A. Labinger, P. Mehrkhodavandi, G. E. Morris, G. J. Sunley, P. Vagner and J. E. Bercaw, *Inorg. Chem.*, 2007, **46**, 11371.
- 29 N. Hazari, J. Labinger, D. Simonetti and E. Iglesia, *Acc. Chem. Res.*, 2012, **45**, 653.
- 30 J. H. Ahn, B. Temel and E. Iglesia, *Angew. Chem.*, 2009, **48**, 3814.
- 31 D. A. Simonetti, J. H. Ahn and E. Iglesia, *J. Catal.*, 2011, **277**, 173.
- 32 D. A. Simonetti, J. H. Ahn and E. Iglesia, *ChemCatChem*, 2011, **3**, 704.
- 33 D. Simonetti, R. T. Carr and E. Iglesia, *J. Catal.*, 2012, **285**, 19.
- 34 M. Sad, M. Neurock and E. Iglesia, *J. Am. Chem. Soc.*, 2011, **133**, 20384.
- 35 D. A. Simonetti and J. A. Dumesic, *Catal. Rev.: Sci. Eng.*, 2009, **51**, 441.
- 36 S. Wang, K. Goulas and E. Iglesia, *J. Catal.*, 2016, **340**, 302.
- 37 S. Wang and E. Iglesia, *J. Phys. Chem. C*, 2016, **120**, 21589.
- 38 T. N. Pham, T. Sooknoi, S. P. Crossley and D. E. Resasco, *ACS Catal.*, 2013, **3**, 2456.
- 39 A. Pulido, B. Oliver-Tomas, M. Renz, M. Boronat and A. Corma, *ChemSusChem*, 2013, **6**, 141.
- 40 S. Wang and E. Iglesia, *J. Catal.*, 2017, **345**, 183.
- 41 T. Yamaguchi and C. Nishimichi, *Catal. Today*, 1993, **16**, 555.
- 42 T. J. Taylor; J. D. Taylor; M. W. Peters and D. E. Henton, *U.S. Pat.* 8,742,187, 2014.
- 43 S. Wang and E. Iglesia, *ACS Catal.*, 2016, **6**, 7664.
- 44 M. L. Sarazen, E. Doskocil and E. Iglesia, *ACS Catal.*, 2016, **6**, 7059.
- 45 M. L. Sarazen, E. Doskocil and E. Iglesia, *J. Catal.*, 2016, **344**, 553.
- 46 K. Tanabe, in *Acid-base bifunctional catalysis*, ed. J. Fraissard and L. Petrakis, Kluwer Academic Publishers, Dordrecht, 1994, p. 353.
- 47 K. Tanabe, *Acid-Base Catalysis*, Kodansha-VCH, 1989.
- 48 J. E. Rekoske and M. A. Barteau, *Ind. Eng. Chem. Res.*, 2011, **50**, 41.
- 49 A. J. Jones and E. Iglesia, *ACS Catal.*, 2015, **5**, 5741.
- 50 S. Wang and E. Iglesia, *ACS Catal.*, submitted.